

Spin-dependent photogalvanic effects (A review)

E.L. Ivchenko¹ and S.D. Ganichev²

¹ *A.F. Ioffe Physico-Technical Institute, Russian Academy of Sciences
194021 St. Petersburg, Russia - ivchenko@coherent.ioffe.ru and*

² *University of Regensburg, Regensburg, 93040 Germany - sergey.ganichev@physik.uni-regensburg.de*

In this paper we review both theoretical and experimental studies on spin-related photogalvanic effects. A short phenomenological introduction is followed by the discussion of the circular photogalvanic effect, the direct and inverse spin-galvanic effects and the trembling motion of spin-polarized electrons. Then we consider the pure spin currents and magneto-gyrotropic photocurrents. Finally, we discuss the spin-dependent photocurrents in topological insulators and Weyl semimetals.

PACS numbers:

I. INTRODUCTION. PHENOMENOLOGICAL DESCRIPTION

The spin of electrons and holes in solid state systems is an intensively studied quantum mechanical property showing a large variety of interesting physical phenomena. One of the most frequently used and powerful methods of generation and investigation of spin polarization is optical orientation [1]. Besides purely optical phenomena like circularly-polarized photoluminescence, the optical generation of an unbalanced spin distribution in a semiconductor may lead to spin photocurrents.

Light propagating through a semiconductor and acting upon mobile carriers can generate a *dc* electric current, under short-circuit condition, or a voltage, in the case of open-circuit samples. In this review we consider only the photogalvanic effects (PGE) which, by definition, appear neither due to inhomogeneity of optical excitation of electron-hole pairs nor due to inhomogeneity of the sample. Moreover, we focus the attention here on the spin-photogalvanics and discuss spin-related mechanisms of the following effects: the circular PGE, spin-galvanic effect, inverse spin-galvanic effect or spin polarization by electric current, generation of pure spin photocurrents and magneto-gyrotropic photogalvanic effect.

The macroscopic features of all spin-dependent PGEs discussed in this article, e.g., the possibility to generate a helicity-dependent current, its behavior upon variation of radiation helicity, crystallographic orientation, experimental geometry etc., can be described in the frame of a phenomenological theory which operates with conventional vectors, or *polar* vectors, and pseudo-vectors, or *axial* vectors describing rotation, and does not depend on details of microscopic mechanisms. Below we consider one by one the phenomenological theory of various spin-photogalvanic effects.

Circular Photogalvanic Effect The signature of photocurrent due to the circular PGE is that it appears only under illumination with circularly polarized light and reverses its direction when the sign of circular polarization is changed. Physically, the circular PGE can be considered as a transformation of the photon angular momenta into a translational motion of free charge

carriers. It is an electronic analog of mechanical systems which transmit rotatory motion to linear one. In general there exist two different possibilities for such transmission. The first is based on the wheel effect: when a wheel being in mechanical contact with the plane surface rotates it simultaneously moves as a whole along the surface. The second transformation is based on the screw effect and exemplified by a screw thread or a propeller. In the both cases the rotation inversion results in the reversal of motion, like the circular photogalvanic current changes its sign following the inversion of the photon helicity described by the degree of circular polarization $P_c = (I_{\sigma_+} - I_{\sigma_-}) / (I_{\sigma_+} + I_{\sigma_-})$, where I_{σ_+} and I_{σ_-} are the intensities of the right-handed (σ_+) and left-handed (σ_-) circularly polarized radiation, respectively.

Phenomenologically, the circular photogalvanic current \mathbf{j} is described by a second-order pseudotensor

$$j_\lambda = I\gamma_{\lambda\mu}i(\mathbf{e} \times \mathbf{e}^*)_\mu = IP_c\gamma_{\lambda\mu}n_\mu, \quad (1)$$

where \mathbf{n} is the unit vector pointing in the direction of the exciting beam, i is the imaginary unity, I and \mathbf{e} are the light intensity and polarization unit vector, for an elliptically polarized light the vector \mathbf{e} is complex. In Eq. (1), the second equality is valid for the transverse electromagnetic wave satisfying the property $i(\mathbf{e} \times \mathbf{e}^*) = P_c\mathbf{n}$. Hereafter a repeated subscript is understood to imply summation over the range of this subscript. In a bulk semiconductor or superlattice the index λ runs over all three Cartesian coordinates x, y, z . In quantum well (QW) structures the free-carrier motion along the growth direction is quantized and the index λ enumerates two in-plane coordinates. In quantum wires the free movement is allowed only along one axis, the principal axis of the structure, and the coordinate λ is parallel to this axis. On the other hand, the light polarization unit vector \mathbf{e} and directional unit vector \mathbf{n} can be arbitrarily oriented in space and, therefore, $\mu = x, y, z$.

The tensor γ in Eq. (1) relates components of the polar vector \mathbf{j} and the axial vector $\mathbf{e} \times \mathbf{e}^*$ which means that it is nonzero for point groups that allow optical activity or *gyrotropy*. We remind that the gyrotropic point group symmetry makes no difference between components of polar vectors, like current or electron momentum, and axial

vectors, like a magnetic field or spin. Among 21 crystal classes lacking inversion symmetry, 18 are gyrotropic; three nongyrotropic noncentrosymmetric classes are T_d , C_{3h} and D_{3h} , for more details see e.g. [2, 3].

Spin-Galvanic and Inverse Spin-Galvanic Effects Another root of spin-photogalvanics is provided by optical spin orientation. A uniform nonequilibrium spin polarization obtained by any means, including optical, yields an electric current if the system is characterized by the gyrotropic symmetry. The current \mathbf{j} and spin \mathbf{S} are also related by a second-order pseudotensor

$$j_\lambda = Q_{\lambda\mu} S_\mu . \quad (2)$$

This equation shows that the direction of the electric current is coupled to the orientation of the nonequilibrium spin which is given by the radiation helicity. The effect inverse to the spin-galvanic effect is an electron spin polarization induced by a *dc* electric current, namely,

$$S_\mu = R_{\mu\lambda} j_\lambda . \quad (3)$$

We note the similarity of Eqs. (1)-(3) characteristic for effects due to gyrotropy: all three equations linearly couple a polar vector with an axial vector.

Pure Spin Photocurrents While describing spin-dependent phenomena, one needs, in addition to electric currents, introduce spin currents. Hereafter we use the notation $q_{\lambda\mu}$ for the spin flux density with μ indicating the spin orientation and λ indicating the flow direction. Of special interest is the generation of pure spin currents in which case a charge current is absent but at least one of the $q_{\lambda\mu}$ components is nonzero. A fourth-order tensor \mathbf{P} relating the pseudotensor \mathbf{q} with the light intensity and polarization as follows

$$q_{\lambda\mu} = IP_{\lambda\mu\nu\eta} e_\nu e_\eta^* \quad (4)$$

has nonzero components in all systems lacking a center of inversion symmetry. However an equivalence between polar and axial vector components in the gyrotropic point groups suggests new important mechanisms of pure spin currents connected with the spin-orbit splitting of electronic bands.

Magneto-Photogalvanic Effects The variety of effects under consideration is completed by magnetic-field induced photocurrents gathered in the class of magneto-photogalvanic effects represented by the phenomenological equation

$$j_\lambda = I\Phi_{\lambda\mu\nu\eta} B_\mu e_\nu e_\eta^* , \quad (5)$$

where \mathbf{B} is an external magnetic field. The symmetry properties of the tensor Φ coincide with those of \mathbf{P} . In this paragraph we will consider a magneto-gyrotropic photocurrent induced by a linearly polarized radiation which can be directly connected with the pure spin current generated at zero magnetic field.

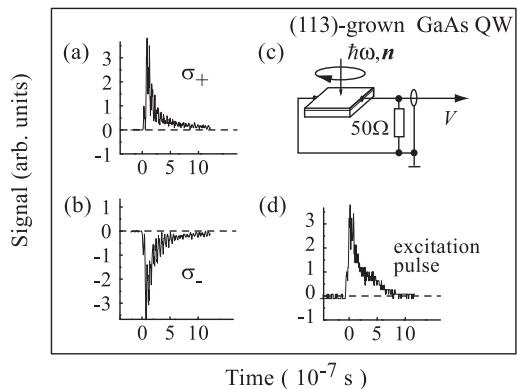


FIG. 1: Oscilloscope traces obtained for pulsed excitation of (113)-grown *n*-type GaAs QWs at $\lambda = 76 \mu\text{m}$. (a) and (b) show circular PGE signals obtained for circular σ_+ and σ_- polarization, respectively. For comparison, in (d) a signal pulse for a fast photon drag detector is plotted. In (c) the measurement arrangement is sketched. After [10].

II. CIRCULAR PHOTO GALVANIC EFFECT

A. Historical Background

The circular photogalvanic effect was independently predicted by Ivchenko and Pikus [4] and Belinicher [5]. It was first observed and studied in tellurium crystals by Asnin et al. [6], see more references in the book [7]. In tellurium the current arises due to spin splitting of the valence band edge at the boundary of the first Brillouin-zone (“camel back” structure). While neither bulk zincblende materials like GaAs and related compounds nor bulk diamond crystals like Si and Ge allow this effect, in QW structures the circular PGE is possible due to a reduction of symmetry. The circular PGE in gyrotropic QWs was observed by Ganichev et al. applying terahertz (THz) radiation [8–10]. In this review we discuss the circular PGE in QW structures grown along the [001], [113] and [110] directions, present experimental data for demonstration and outline the microscopic theory of the effect under intersubband and interband optical transitions.

B. Basic Experiments

With illumination of QW structures by polarized radiation a current signal proportional to the helicity P_c is generated in unbiased samples. The irradiated structure represents a current source wherein the current flows in the QW, see a scheme in Fig. 1(c). Figures 1(a) and 1(b) show measurements of the voltage drop across a 50 Ohm load resistor in response to 100 ns laser pulses at $\lambda = 76 \mu\text{m}$. Signal traces are plotted for right-handed (a) and left-handed circular polarization (b), in comparison to a reference signal shown in Fig. 1(d) and obtained from a fast photon drag detector [10, 11]. The width of the cur-

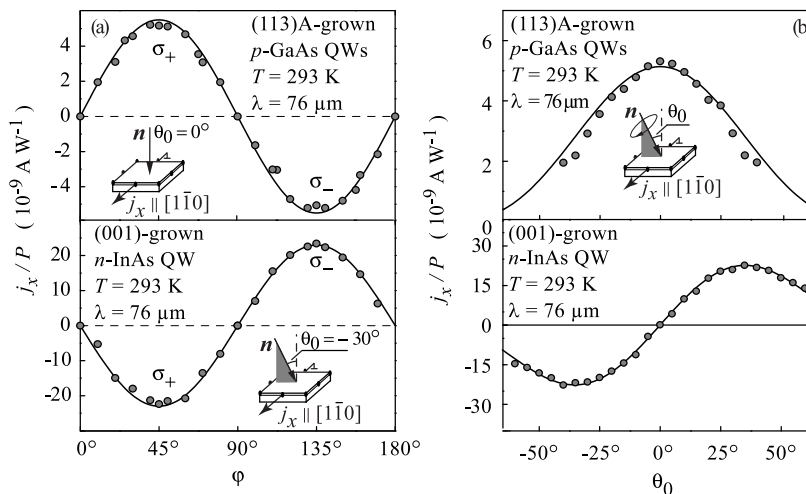


FIG. 2: (a) Photocurrent in QWs normalized by the light power P as a function of the phase angle φ defining the helicity. *Upper panel:* normal incidence of radiation on p -type (113)-grown GaAs/AlGaAs QWs (symmetry class C_s). The current j_x flows along the $[1\bar{1}0]$ direction perpendicular to the mirror plane. *Lower panel:* oblique incidence of radiation with an angle of incidence $\theta_0 = -30^\circ$ on n -type (001)-grown InAs/AlGaSb QWs (symmetry class C_{2v}). Full lines are fitted using one parameter according to Eq. (7). (b) Photocurrent as a function of the incidence angle θ_0 for right-circularly polarized radiation σ_+ measured perpendicularly to light propagation. *Upper panel:* p -type (113)-grown GaAs/AlGaAs QWs. *Lower panel:* n -type (001)-grown InAs/AlGaSb QWs. Full lines represent theoretical fit. The insets show the geometry of the experiment, \mathbf{n} is the directional unit vector. After [9].

rent pulses is about 100 ns which corresponds to the THz laser pulses duration.

Figure 2(a) presents results of measurements carried out at room temperature on (113)-grown p -GaAs/AlGaAs multiple QWs under normal incidence and (001)-grown n -InAs/AlGaSb single QW structure under oblique incidence. Optical excitation was performed by a high-power THz pulsed NH_3 laser operating at wavelength $\lambda = 76 \mu\text{m}$. The linearly polarized light emitted by the laser could be modified to an elliptically polarized radiation by applying a $\lambda/4$ plate and changing the angle φ between the optical axis of the plate and the polarization plane of the laser radiation. Thus the helicity P_c of the incident light varies from -1 (left handed, σ_-) to $+1$ (right handed, σ_+) according to

$$P_c = \sin 2\varphi. \quad (6)$$

One can see from Fig. 2(a) that the photocurrent direction is reversed when the polarization switches from right-handed circular, $\varphi = 45^\circ$, to left-handed, $\varphi = 135^\circ$. The experimental points are well fitted by the equation

$$j_\lambda(\varphi) = j_C \sin 2\varphi \quad (7)$$

with one scaling parameter. While in some systems and experimental conditions the total photocurrent originates solely from the circular PGE, like for the data in Fig. 2(a), in most cases it is accompanied by the contributions caused by the linear photogalvanic or photon drag effects [2, 11]. The latter are out of scope of this review focused on the spin photogalvanics. The additional contributions, however, complicate the dependence of the

photocurrent on the radiation polarization state which in a general case is given by

$$j_\lambda(\varphi) = j_C \sin 2\varphi + j_{L1} \sin 4\varphi + j_{L2} \cos 4\varphi + j_{\text{offset}}. \quad (8)$$

The circular photocurrent, being proportional to P_c , can easily be extracted from the total current by subtracting the photocurrents excited by the σ_+ and σ_- circularly polarized radiation.

In Fig. 2(b) closer look is taken at the dependence of the photocurrent on the angle of incidence θ_0 in configuration with the incidence plane normal to the axis $x \parallel [1\bar{1}0]$.

For (113)-oriented QWs belonging to the symmetry class C_s the current retains its sign for all θ_0 and achieves its maximum at normal incidence, see upper panel of Fig. 2(b). In contrast, in asymmetric (001)-oriented samples (C_{2v} -symmetry) a variation of θ_0 in the plane of incidence normal to x changes the sign of the current j_x for normal incidence, $\theta_0=0$, as can be seen in the lower panel of Fig. 2(b). Solid curves in this figure show a fit with phenomenological equation (1) adapted to a corresponding symmetry and being in a good agreement with experiment.

Further experiments demonstrate that circular PGE can be generated by the radiation of wide range of frequencies from terahertz to visible light. Applying light of various frequencies the photocurrent due to interband, intersubband and free carrier absorption was detected.

Absorption of radiation in the range of 9 to 11 μm in n -type GaAs QW samples of well widths $8 \div 9 \text{ nm}$ is dominated by resonant direct intersubband optical transitions

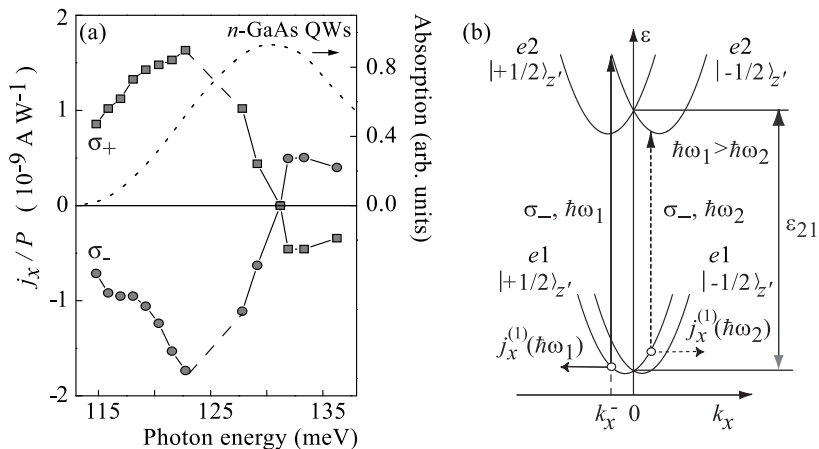


FIG. 3: (a) Photocurrent in QWs normalized by the light power P as a function of the photon energy $\hbar\omega$. Measurements are presented for n -type (001)-grown GaAs/AlGaAs QWs of 8.2 nm width at room temperature. Oblique incidence of σ_+ (squares) and σ_- (circles) circularly polarized radiation with an angle of incidence $\theta_0 = 20^\circ$ was used. The current j_x was measured perpendicular to the light incidence plane (y, z). The dotted line shows the absorption measurement using a Fourier transform infrared spectrometer. After [12]. (b) Microscopic picture describing the origin of the circular photogalvanic current and its spectral inversion in C_s point group samples. The essential ingredient is the splitting of the conduction band due to \mathbf{k} -linear terms. Left handed circularly polarized radiation σ_- induces direct spin-flip transitions (vertical arrows) from the $e1$ subband with $s = 1/2$ to the $e2$ subband with $s' = -1/2$. As a result an unbalanced occupation of the k_x states occurs yielding a spin polarized photocurrent. For transitions with k_x^- lying left to the minimum of $e1$ ($s = 1/2$) subband the current indicated by j_x is negative. At smaller ω the transition occurs at a value of k_x on the right-hand side of the subband minimum, and the current reverses its sign. After [12].

between the first ($e1$) and the second ($e2$) size-quantized subbands.

Applying mid-infrared (MIR) radiation from the CO_2 laser, which causes direct transitions in GaAs QWs, a current signal proportional to the helicity P_c has been observed at normal incidence in (113)-oriented samples and (110)-grown asymmetric QWs and at oblique incidence in (001)-oriented samples, indicating a spin orientation induced circular PGE [12, 13]. In Fig. 3(a) the data are presented for a (001)-grown n -type GaAs QW of 8.2 nm width measured at room temperature. It is seen that the current for both left- and right-handed circular polarization changes sign at the frequency of the absorption peak. Spectral inversion of the photocurrent direction at intersubband resonance has also been observed in (113)-oriented samples and (110)-grown asymmetric QWs [12, 13].

While in all above cases the geometry required for the photocurrent is forced by symmetry arguments, in the systems of C_1 point-group symmetry (containing only the identity operation), e.g. in (013)-oriented QWs, the space symmetry imposes no restriction on the relation between radiation electric field and photocurrent components resulting in a complex spectral and temperature behaviour [14].

C. Microscopic Model for Intersubband Transitions

We start the microscopic consideration from the inter-

subband mechanism of circular PGE. Microscopically, as shown below, a conversion of photon helicity into a current as well as a number of effects described in this review is due to a removal of spin degeneracy in the \mathbf{k} -space resulting in a shift of two spin subbands as sketched in Fig. 3(b). Thus before a discussion of the photocurrent origin we briefly describe the band spin splitting.

D. Relation to

The linear in \mathbf{k} terms in the Hamiltonian are given by the contribution

$$\mathcal{H}_{\mathbf{k}}^{(1)} = \beta_{\mu\lambda} \sigma_{\mu} k_{\lambda} \quad (9)$$

to the expansion of the electron effective Hamiltonian in powers of the wave vector \mathbf{k} . The coefficients $\beta_{\mu\lambda}$ form a pseudotensor subjected to the same symmetry restriction as the current-to-spin tensor \mathbf{R} or the transposed pseudotensors $\boldsymbol{\gamma}$ and \mathbf{Q} . The coupling between the electron spin and momentum described by products of the Pauli spin matrices σ_{μ} and the wave vector components k_{λ} as well as spin-dependent selection rules for optical transitions yield a net current sensitive to circularly polarized optical excitation. The first source of \mathbf{k} -linear terms is the bulk inversion asymmetry (BIA), the corresponding contribution to (9) is obtained by quantum-mechanical averaging [15] of the cubic-in- \mathbf{k} Hamiltonian introduced by Dresselhaus [16]. The spin-orbit splitting also arises from a structure inversion asymmetry (SIA),

see Refs. [10, 17–20]. The breakdown of reduced symmetry at an interface, or the interface inversion asymmetry (IIA), leads to a renormalization of the BIA contribution [21–23]. The second-rank pseudotensors β , R , γ and Q for QW structures of different crystallographic orientations as well as application of the spin photocurrents for studying the BIA and SIA anisotropy are reviewed in Ref. [24].

E. Circular PGE Due to Intersubband Transitions

Figure 3(b) illustrates the intersubband transitions $e1 \rightarrow e2$ resulting in the circular PGE. In order to make the physics more transparent we will first consider the intersubband circular photogalvanic current generated under normal incidence in QWs of the C_s symmetry, say, in (113)-grown QWs, and use the relevant coordinate system $x \parallel [1\bar{1}0]$, $y' \parallel [3\bar{3}2]$, $z' \parallel [113]$. In the linear- \mathbf{k} Hamiltonian we retain only the term $\sigma_{z'}k_x$ because other terms make no contribution to the photocurrent under the normal incidence. Therefore, the energy dispersion in the ν th electron subband depicted in Fig 3(b) is taken as

$$E_{e\nu, \mathbf{k}, s} = E_\nu^0 + \frac{\hbar^2 k^2}{2m_c} + 2s\beta_\nu k_x, \quad (10)$$

where $s = \pm 1/2$ is the electron spin component along the z' axis, $\beta_\nu = \beta_{z'x}^{(\nu)}$ and, for the sake of simplicity, we neglect nonparabolicity effects assuming the effective mass m_c to be the same in both subbands.

For the direct $e1$ - $e2$ transitions shown in Fig 3 by vertical arrows, the energy and momentum conservation laws read

$$E_{21} + 2(s'\beta_2 - s\beta_1)k_x = \hbar\omega,$$

where E_{21} is the Γ -point gap $E_2^0 - E_1^0$ and s' , $s = \pm 1/2$. As a result of optical selection rules the circular polarization, e.g., left-handed, under normal incidence induces direct optical transitions between the subband $e1$ with spin $s = +1/2$ and the subband $e2$ with spin $s' = -1/2$. For monochromatic radiation with photon energy $\hbar\omega_1 > E_{21}$ optical transitions occur only at a fixed value of k_x^- where the energy of the incident light matches the transition energy as indicated by the arrow in Fig. 3(b). Therefore, optical transitions induce an imbalance of the momentum distribution in both subbands yielding an electric current along the x -direction with the $e1$ and $e2$ contributions, antiparallel ($\mathbf{j}^{(1)}$) or parallel ($\mathbf{j}^{(2)}$) to x , respectively. Since in n -type QWs the energy separation between the $e1$ and $e2$ subbands is typically larger than the energy of longitudinal optical phonons $\hbar\omega_{LO}$, the nonequilibrium distribution of electrons in the $e2$ subband relaxes rapidly due to emission of phonons. As a result, the electric current $\mathbf{j}^{(2)}$ vanishes and the current magnitude and direction are determined by the group velocity and the momentum relaxation time τ_p of uncompensated electrons in the $e1$ subband with $s = +1/2$, i.e.,

by $\mathbf{j}^{(1)}$. By switching circular polarization from left- to right-handed due to selection rules light excites the spin down subband only.

Thus the whole picture mirrors and the current direction reverses. Spectral inversion of the photocurrent at fixed helicity also follows from the model picture of Fig. 3(b). Indeed decreasing the photon frequency to $\hbar\omega_2 < E_{21}$ shifts the transitions toward positive k_x and the direction of the current reverses (horizontal dashed arrow).

Formally this process is described as follows. In the polarization $\mathbf{e} \perp z'$, the direct intersubband absorption is weakly allowed only for the spin-flip transitions, $(e1, -1/2) \rightarrow (e2, 1/2)$ for σ_+ photons and $(e1, 1/2) \rightarrow (e2, -1/2)$ for σ_- photons. Particularly, under the σ_- photoexcitation the electrons involved in the transitions have the fixed x -component of the wave vector

$$k_x^- = -\frac{\hbar\omega - E_{21}}{\beta_2 + \beta_1} \quad (11)$$

and velocity

$$v_x^{(e\nu)} = \frac{\hbar k_x^-}{m_c} + (-1)^{\nu+1} \frac{\beta_\nu}{\hbar}. \quad (12)$$

The circular photogalvanic current can be written as

$$j_x^{(e1)} = e \left(v_x^{(e2)} \tau_p^{(2)} - v_x^{(e1)} \tau_p^{(1)} \right) \frac{\eta_{21} I}{\hbar\omega} P_c, \quad (13)$$

where $\tau_p^{(\nu)}$ is the electron momentum relaxation time in the ν subband, η_{21} is the absorbance or the fraction of the energy flux absorbed in the QW due to the transitions under consideration, and minus in the right-hand side means that the $e1$ -electrons are removed in the optical transitions.

We assume that inhomogeneous broadening, δ_{21} , of the resonance E_{21} exceeds, by far, the subband spin splitting. In this case the convolution of the current given by Eq. (13) with the inhomogeneous distribution function leads to [12]

$$j_x = \frac{e}{\hbar} (\beta_2 + \beta_1) \left[\tau_p^{(2)} \eta_{21} (\hbar\omega) + (\tau_p^{(1)} - \tau_p^{(2)}) \langle E \rangle \frac{d\eta_{21}(\hbar\omega)}{d\hbar\omega} \right] \frac{IP_c}{\hbar\omega}, \quad (14)$$

where η_{21} is the absorbance in the polarization $\mathbf{e} \perp z'$ calculated neglecting the linear- \mathbf{k} terms but taking into account the inhomogeneous broadening, $\langle E \rangle$ is the mean value of the two-dimensional (2D) electron energy, namely half of the Fermi energy E_F for a degenerate 2D electron gas and $k_B T$ for a nondegenerate gas. Since the derivative $d\eta_{21}/d(\hbar\omega)$ changes its sign at the absorption peak frequency and usually the time $\tau_p^{(1)}$ is much longer than $\tau_p^{(2)}$, the circular photogalvanic current given by Eq. (14) exhibits the sign-inversion behavior within the resonant absorption contour, in agreement with the experimental observations [12, 13].

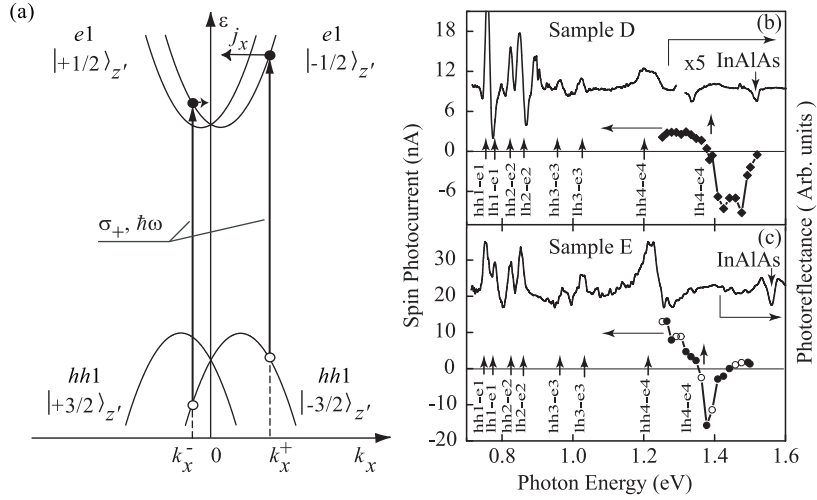


FIG. 4: (a) Microscopic picture describing the origin of interband circular PGE. The essential ingredient is the spin splitting of the electron and/or hole states due to linear- \mathbf{k} terms. (b)-(c) Spectral response of the circular photogalvanic current observed in two (001)-grown $\text{In}_x\text{Ga}_{1-x}\text{As}/\text{InAlAs}$ QW structures, sample D and sample E, under oblique incidence. To enhance the structure inversion asymmetry, sample E was grown with a graded indium composition from 0.53 to 0.75 for the QW, instead of the uniform indium composition of 0.70 for sample D. The photoreflectance spectra of two samples are also shown to determine the electronic structures of the samples. The arrows indicate the heavy hole (hh) and light hole (lh) related transitions. Data are given after [27].

Similarly to the previously discussed case of the C_s symmetry the circular photogalvanic current for the $e1$ - $e2$ transitions in (001)-grown QWs exhibits the sign-inversion behavior within the resonant absorption contour [12], in agreement with the experimental data presented in Fig. 3(a).

F. Interband Optical Transitions

For direct optical transitions between the heavy-hole valence subband $hh1$ and conduction subband $e1$, the circular PGE is also most easily conceivable in QWs of the C_s symmetry which allows the spin-orbit term $\beta_{z'x}\sigma_{z'}k_x$. We assume the parabolic dispersion in the conduction and heavy-hole subbands, $e1$ and $hh1$ respectively, taking into account the linear- \mathbf{k} terms as follows

$$E_{e1,\mathbf{k},\pm 1/2} = E_g^{QW} + \frac{\hbar^2 k^2}{2m_c} \pm \beta_e k_x, \quad (15)$$

$$E_{hh1,\mathbf{k},\pm 3/2}^v = -\frac{\hbar^2 k^2}{2m_v} \pm \beta_h k_x,$$

where m_v is the hole in-plane effective mass, $\beta_e = \beta_{z'x}^{(e1)}$, $\beta_h = \beta_{z'x}^{(hh1)}$, E_g^{QW} is the band gap renormalized because of the quantum confinement of free carriers and the energy is referred to the valence-band top. In Fig. 4(a) the allowed optical transitions are from $j = -3/2$ to $s = -1/2$ for the σ_+ polarization and from $j = 3/2$ to $s = 1/2$ for the σ_- polarization. Under circularly polarized radiation with a photon energy $\hbar\omega$ and for a fixed value of k_y , the energy and momentum conservation allow transitions only from two values of k_x labeled k_x^- and

k_x^+ . The corresponding transitions are shown in Fig. 4(a) by the solid vertical arrows with their “center-of-mass” shifted from the point $k_x = 0$.

Thus the average electron velocity in the excited state is nonzero and the contributions of k_x^\pm photoelectrons to the current do not cancel each other as in the case $\beta_e = \beta_h = 0$. Changing the photon helicity from $+1$ to -1 inverts the current because the “center-of-mass” for these transitions is now shifted in the opposite direction. The asymmetric distribution of photoelectrons in the \mathbf{k} -space decays within the momentum relaxation time. However, under steady-state optical excitation new photocarriers are generated resulting in a dc photocurrent. The photohole contribution is considered in a similar way. The final result for the interband circular photogalvanic current can be presented as

$$j_x = -e(\tau_p^e - \tau_p^h) \left(\frac{\beta_e}{m_v} + \frac{\beta_h}{m_c} \right) \frac{\mu_{cv} \eta_{eh} I}{\hbar \hbar\omega} P_c, \quad (16)$$

where η_{eh} is the fraction of the photon energy flux absorbed in the QW due to the $hh1 \rightarrow e1$ transitions and τ_p^e, τ_p^h are the electron and hole momentum relaxation times.

The circular PGE at interband absorption was observed in GaAs-, InAs- and GaN-based QW structures [25–31] and bulk semiconductors InN [32] and BiTeBr [33]. In Figs. 4(b) and 4(c) diamonds and circles present the spectral dependence of the circular photogalvanic current measured under interband optical transitions between the higher valence and conduction subbands. The photo-reflectance spectra of the samples are shown (solid curves) to clearly indicate the quantized energy levels of electrons and holes as marked by the arrows.

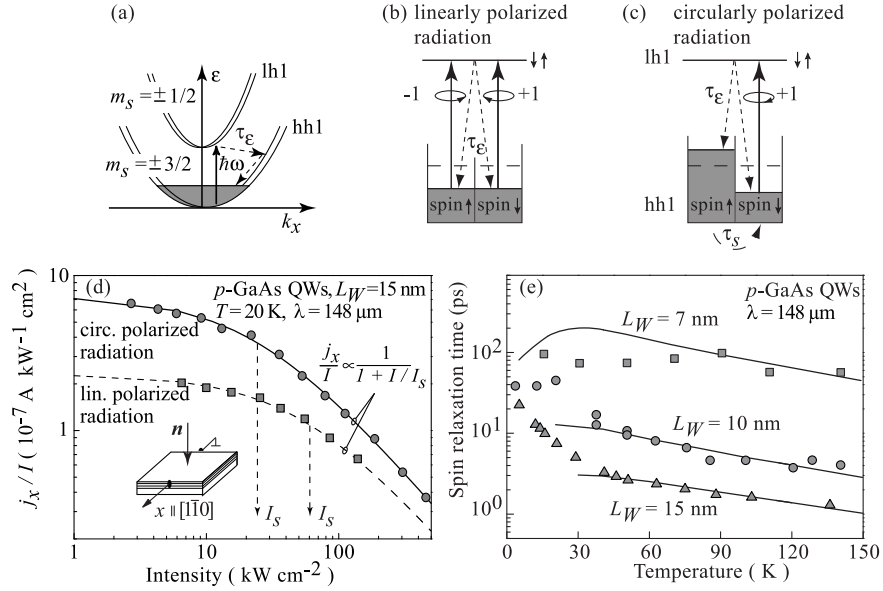


FIG. 5: (a)-(c) Microscopic picture of spin sensitive bleaching: Direct $hh1$ - $lh1$ optical transitions (a) and process of bleaching for two polarizations, linear (b) and circular (c). Dashed arrows indicate energy (τ_ε) and spin (τ_s) relaxation. (d) Circular (squares) and linear PGE (circles) currents j_x normalized by the intensity as a function of the intensity for circularly and linearly polarized radiation. The inset shows the geometry of the experiment. The measurements are fitted to $j_x/I \propto 1/(1+I/I_s)$ with one parameter I_s for each state of polarization. Data are given for (113)-grown samples after [37]. (e) Spin relaxation times of holes for three different widths of (113)-grown GaAs/AlGaAs QWs as a function of temperature. The solid lines show a fit according to the Dyakonov–Perel relaxation mechanism. After [38].

For the both samples the photocurrent spectral contour exhibits a change in sign, in a qualitative agreement with the theoretical prediction [34].

In addition to the interband and intersubband photocurrents, the circular PGE can be caused by intra-band (or intrasubband) mechanisms [9]. In Refs. [35, 36], a semiclassical theory of nonlinear transport and intra-band photogalvanic effects has been proposed for noncentrosymmetric media, and the orbital Berry-phase contribution to helicity-dependent photocurrents has been computed.

G. Spin-Sensitive Bleaching

Application of high intensities results in saturation (bleaching) of PGE. This effect was observed for direct intersubband transitions in p -type GaAs QWs and gave an experimental access to spin relaxation times [37, 38]. The method is based on the difference in nonlinear behavior of circular and linear PGE. We remind that the linear PGE is another photogalvanic effect allowed in GaAs structures and can be induced by linearly polarized light [2, 7, 11]. Both currents are proportional to absorption and their nonlinear behavior reflects the nonlinearity of absorbance.

Spin sensitive bleaching can be analyzed in terms of a simple model taking into account both optical excitation and nonradiative relaxation processes. Excitation with THz radiation results in direct transitions be-

tween heavy-hole ($hh1$) and light-hole ($lh1$) subbands, see Fig. 5(a). This process depopulates and populates selectively spin states in the $hh1$ and $lh1$ subbands. The absorption is proportional to the difference of populations of the initial and final states. At high intensities the absorption decreases since the photoexcitation rate becomes comparable to the nonradiative relaxation rate to the initial state.

Absorption of linearly polarized light is not spin selective and the saturation is controlled by energy relaxation, Fig. 5(b). In contrast, absorption of circularly polarized light is spin selective due to selection rules, and only one type of spin is excited, Fig. 5(c). Note that during energy relaxation the hot holes lose their photoinduced orientation due to rapid relaxation so that the spin orientation occurs only within the bottom of the $hh1$ subband. Thus the absorption bleaching of circularly polarized radiation is governed by energy relaxation of photoexcited carriers and spin relaxation within the subband $hh1$. These processes are characterized by energy and spin relaxation times, τ_ε and τ_s , respectively. If τ_s is longer than τ_ε the bleaching of absorption becomes spin sensitive and the saturation intensity of circularly polarized radiation drops below the value of linear polarization.

Bleaching of absorption with increasing the intensity of linearly polarized light is described phenomenologically by the function

$$\eta(I) = \frac{\eta_0}{1 + I/I_{se}}, \quad (17)$$

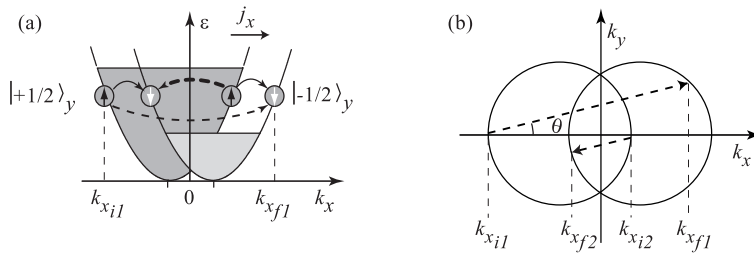


FIG. 6: Microscopic origin of the spin-galvanic current. (a) One-dimensional sketch: the $\sigma_y k_x$ term in the Hamiltonian splits the conduction band into two parabolas with the spin $s_y = \pm 1/2$ pointing in the y -direction. If one of the spin-split subbands is preferentially occupied, e.g., by spin injection ($|+1/2\rangle_y$ -states in the figure), spin-flip scattering results in a current in the x -direction. The scattering rate depends on values of the initial and final electron wave vectors. Thus, the transitions sketched by dashed arrows yield an asymmetric filling of the subbands and, hence, a current flow. If instead of the spin-up subband the spin-down subband is preferentially occupied, the current direction is reversed. (b) The spin-flip transitions in the two dimensions at scattering angle θ different from zero. After [10, 41].

where $\eta_0 = \eta(I \rightarrow 0)$ and I_{se} is the characteristic saturation intensity controlled by energy relaxation of the 2D hole gas. Since the photocurrent of linear PGE, j_{LPGE} , induced by the linearly polarized light is proportional to ηI , one has

$$\frac{j_{LPGE}}{I} \propto \frac{1}{1 + I/I_{se}}. \quad (18)$$

The circular photogalvanic current j_{CPGE} induced by the circularly polarized radiation is proportional to the degree of hole spin polarization and given by [37]

$$\frac{j_{CPGE}}{I} \propto \frac{1}{1 + I(I_{se}^{-1} + I_{ss}^{-1})}, \quad (19)$$

where $I_{ss} = p_s \hbar \omega / (\eta_0 \tau_s)$, p_s is the 2D hole density.

The measurements illustrated in Fig. 5(d) indicate that the photocurrent j_x at a low power level depends linearly on the light intensity and gradually saturates with increasing intensity, $j_x \propto I/(1 + I/I_s)$, where I_s is the saturation parameter. One can see from Fig. 5(d) that the measured saturation intensity for circular polarized radiation is smaller than that for linearly polarized light. Using the measured values of I_s and Eqs. (18) and (19) one can estimate the parameter I_{ss} and even the time τ_s [37, 38].

Figure 5(e) presents spin relaxation times extracted from experiment (points) together with a theoretical fit assuming that the Dyakonov–Perel mechanism [39] of hole spin relaxation is dominant.

III. SPIN-GALVANIC EFFECT

The mechanisms of circular PGE discussed so far are linked with the asymmetry in the momentum distribution of carriers excited in optical transitions which are sensitive to the light circular polarization due to selection rules. Now we discuss an additional possibility to generate a photocurrent sensitive to the photon helicity. In a

system of free carriers with nonequilibrium spin-state occupation but equilibrium energy distribution within each spin branch, the spin relaxation can be accompanied by generation of an electric current. This effect, predicted by Ivchenko et al.[40], was observed by Ganichev et al. applying THz radiation and named the spin-galvanic effect [41].

If the nonequilibrium spin is produced by optical orientation proportional to the degree of light circular polarization P_C the current generation can be reputed just as another mechanism of the circular PGE. However the nonequilibrium spin \mathbf{S} can be achieved both by optical and non-optical methods, e.g., by electrical spin injection, and, in fact, Eq. (2) presents an independent effect.

Usually the circular PGE and spin-galvanic effect are observed simultaneously under illumination by circularly polarized light and do not allow an easy experimental separation. However, they can be separated in time-resolved measurements. Indeed, after removal of light or under pulsed photoexcitation the circular photogalvanic current decays within the momentum relaxation time τ_p whereas the spin-galvanic current decays with the spin relaxation time.

Another method which, on the one hand, provides a uniform distribution in spin subbands and, on the other hand, excludes the circular PGE was proposed in Ref. [41]. It is based on the use of optical excitation and the assistance of an external magnetic field to achieve an in-plane polarization in (001)-grown low-dimensional structures. Finally we note that the spin-galvanic effect and its inversion, see Sect. IV, have been detected in electron transport experiments which do not imply optical excitation and, therefore, are out of scope of this review.

A. Microscopic Mechanisms

For (001)-grown asymmetric QWs characterized by the C_{2v} symmetry only two linearly independent components, Q_{xy} and Q_{yx} , of the tensor \mathbf{Q} in Eq. (2) are

nonzero so that

$$j_x = Q_{xy}S_y, \quad j_y = Q_{yx}S_x. \quad (20)$$

Hence, a spin polarization driven current needs a spin component lying in the QW plane. For the C_s symmetry of (hhl)-oriented QWs, particularly, (113) and asymmetric (110), an additional tensor component $Q_{xz'}$ is nonzero and the spin-galvanic current may be caused by nonequilibrium spins oriented normally to the QW plane.

Figure 6 illustrates the generation of a spin-galvanic current. As already addressed above, it arises due to \mathbf{k} -linear terms in the electron effective Hamiltonian, see Eq. (9). For a 2D electron gas system, these terms lead to the situation sketched in Fig. 6(a). More strictly, the scattering changes both k_x and k_y components of the electron wave vector as shown Fig. 6(b) by dashed lines. However, the one-dimensional sketch in 6(a) conveys the interpretation in a simpler and clearer way. In the figure the electron energy spectrum along k_x with allowance for the spin-dependent term $\beta_{yx}\sigma_y k_x$ is shown. In this case $s_y = \pm 1/2$ is a good quantum number. The electron energy band splits into two subbands which are shifted in the \mathbf{k} -space, and each of the bands comprises states with spin up or down. Spin orientation in the y -direction causes the unbalanced population in spin-down and spin-up subbands. As long as the carrier distribution in each subband is symmetric around the subband minimum point no current flows.

As illustrated in Fig. 6(a) the current flow is caused by \mathbf{k} -dependent spin-flip relaxation processes. Spins oriented in the y -direction are scattered along k_x from the more populated spin subband, e.g., the subband $|+1/2\rangle_y$, to the less populated subband $|-1/2\rangle_y$. Four different spin-flip scattering events are sketched in Fig. 6(a) by bent arrows. The spin-flip scattering rate depends on the values of wave vectors of the initial and final states[42]. Therefore, the spin-flip transitions shown by solid arrows in Fig. 6(a) have the same rates. They preserve the symmetric distribution of carriers in the subbands and, thus, do not yield a current. However, two other scattering processes shown by broken arrows are inequivalent and generate an asymmetric carrier distribution around the subband minima in both subbands. This asymmetric population results in a current flow along the x -direction.

The occurrence of a current is due to the spin dependence of the electron scattering matrix elements $\hat{M}_{\mathbf{k}'\mathbf{k}} = A_{\mathbf{k}'\mathbf{k}}\hat{I} + \boldsymbol{\sigma} \cdot \mathbf{B}_{\mathbf{k}'\mathbf{k}}$, where $A_{\mathbf{k}'\mathbf{k}}^* = A_{\mathbf{k}\mathbf{k}'}$, $B_{\mathbf{k}'\mathbf{k}}^* = B_{\mathbf{k}\mathbf{k}'}$ due to hermicity of the interaction and $A_{-\mathbf{k}',-\mathbf{k}} = A_{\mathbf{k}\mathbf{k}'}$, $B_{-\mathbf{k}',-\mathbf{k}} = -B_{\mathbf{k}\mathbf{k}'}$ due to the symmetry under time inversion. Within the model of elastic scattering the current is not spin polarized since the same number of spin-up and spin-down electrons move in the same direction with the same velocity. The spin-galvanic current can be estimated by [43]

$$j_x = Q_{xy}S_y \sim en_s \frac{\beta_{yx}}{\hbar} \frac{\tau_p}{\tau'_s} S_y, \quad (21)$$

and the similar equation for j_y , where n_s is the 2D electron density, τ'_s is the spin relaxation time due to the Elliott–Yafet mechanism [1, 44, 45]. Since spin-flip scattering is the origin of the current given by Eq. (21), this equation is valid even if the Dyakonov–Perel mechanism [1, 39] of spin relaxation dominates. The Elliott–Yafet relaxation time τ'_s is proportional to the momentum relaxation time τ_p . Therefore the ratio τ_p/τ'_s in Eq. (21) does not depend on the momentum relaxation time. The in-plane average spin, e.g., S_y in Eq. (21), decays with the total spin relaxation time τ_s and, hence, the time decay of the spin-galvanic current following pulsed photoexcitation is described by the exponential function $\exp(-t/\tau_s)$. In contrast, the circular PGE current induced by a short-pulse decays within the momentum relaxation time τ_p allowing to distinguish these two effects in time resolved measurements.

In general, in addition to the kinetic contribution to the current there exists the so-called relaxational contribution which arises due to the linear- \mathbf{k} terms neglecting the Elliott–Yafet spin relaxation, i.e., with allowance for the Dyakonov–Perel mechanism only. This contribution has the form

$$\mathbf{j} = -en_s\tau_p\nabla_{\mathbf{k}}\left(\Omega_{\mathbf{k}}^{(1)}\dot{\mathbf{S}}\right), \quad (22)$$

where the spin rotation frequency $\Omega_{\mathbf{k}}^{(1)}$ is defined by $\mathcal{H}^{(1)} = (\hbar/2)\boldsymbol{\sigma}\Omega_{\mathbf{k}}^{(1)}$, i.e., $\hbar\Omega_{\mathbf{k},\mu}^{(1)} = 2\beta_{\mu\lambda}k_\lambda$, and $\dot{\mathbf{S}}$ is the spin generation (or production) rate.

For optical transitions excited under oblique incidence of the light in n -type zinc-blende-lattice QWs of the C_{2v} symmetry, the spin-galvanic effect coexists with the circular PGE described in Section II. In the case of inter-subband transitions in (001)-grown QWs, the spin orientation is generated by resonant spin-dependent and spin-conserving photoexcitation followed by energy relaxation of the photoelectrons from the subband $e2$ to $e1$ and their further thermalization within the subband $e1$. The resulting spin generation rate is given by a product of the optical transition rate times the factor of depolarization, ξ , of the thermalizing electrons, and the current j_x is estimated as

$$j_x \sim e \frac{\beta_{yx}}{\hbar} \frac{\tau_p\tau_s}{\tau'_s} \frac{\eta_{21}I}{\hbar\omega} P_c\xi n_y, \quad (23)$$

where η_{21} is the absorbance under the direct transitions $e1 \rightarrow e2$. Equation (23) shows that the spin-galvanic current is proportional to the absorbance and determined by the spin splitting constant in the first subband, β_{yx} or β_{xy} . This is in contrast to the circular PGE which is proportional to the absorbance derivative, see Eq. (14).

Finally we note that besides spin-flip mechanisms of the current generation the spin-galvanic effect can be caused by the interference of spin-preserving scattering and spin relaxation processes in a system of spin-polarized two-dimensional carriers [46]. Burkov et al. [47] have incorporated the spin-galvanic effect into a set

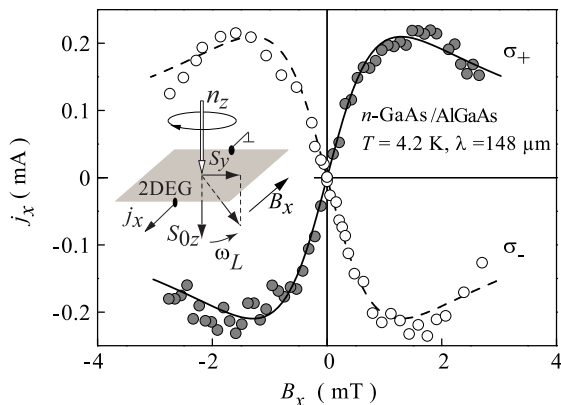


FIG. 7: Spin-galvanic current j_x as a function of magnetic field $\mathbf{B} \parallel x$ for normally incident right-handed (open circles) and left-handed (solid circles) circularly polarized radiation. Solid and dashed curves are fitted after Eqs. (20) and (24) using the same value of the spin relaxation time τ_s and scaling of the ordinate. Inset shows optical scheme of generating a uniform in-plane spin polarization which causes a spin-galvanic current. Electron spins are oriented normal to the QW plane by circularly polarized radiation and rotated into the plane by the Larmor precession in an in-plane magnetic field B_x . After [41].

of equations that provide a description of coupled spin and charge diffusive transport in a two-dimensional electron gas with the SIA spin-orbit interaction.

B. Spin-Galvanic Photocurrent Induced by the Hanle Effect

The spin-galvanic effect can be investigated by pure optical spin orientation due to absorption of circularly polarized radiation in QWs. However, the irradiation of QWs with circularly polarized light also results in the circular PGE, and an indivisible mixture of both effects may be observed since phenomenologically they are described by the tensors, γ and \mathbf{Q} , equivalent from the symmetry point of view. Nevertheless, microscopically these two effects are definitely inequivalent. Indeed, the spin-galvanic effect is caused by asymmetric spin-flip scattering of spin polarized carriers and determined by the spin relaxation processes. If spin relaxation is absent the spin-galvanic current vanishes. In contrast, the circular PGE is a result of selective photoexcitation of carriers in the \mathbf{k} -space with circularly polarized light due to optical selection rules, it is independent of the spin relaxation if $\tau_s \gg \tau_p$.

Here we describe a method which, on the one hand, achieves a uniform distribution of nonequilibrium spin polarization by optical means and, on the other hand, excludes the circular PGE [41]. The polarization is obtained by absorption of circularly polarized radiation at normal incidence on (001)-grown QWs as depicted in the inset in Fig. 7. For normal incidence the spin-galvanic

effect as well as the circular PGE vanish because both $S_x = S_y = 0$ and $n_x = n_y = 0$. Thus, the spin orientation S_{0z} along the z -axis is achieved but no spin-induced photocurrent is generated, in difference with QWs of other crystallographic orientations, e.g. (110), (113) or (013).

An in-plane spin component, necessary for the spin-galvanic effect in (001) oriented QWs, arises in a magnetic field $\mathbf{B} \parallel x$. The field perpendicular to the initially oriented spins rotates them into the plane of the 2D electron gas due to the Larmor precession (Hanle effect). The nonequilibrium spin polarization S_y is given by

$$S_y = -\frac{\omega_L \tau_{s\perp}}{1 + (\omega_L \tau_s)^2} S_{0z}, \quad (24)$$

where $\tau_s = \sqrt{\tau_{s\parallel} \tau_{s\perp}}$, $\tau_{s\parallel}$ and $\tau_{s\perp}$ are the longitudinal and transversal electron spin relaxation times, and ω_L is the Larmor frequency. Since in the experimental set-up $\dot{\mathbf{S}}$ is parallel to z , the scalar product $(\mathbf{\Omega}_k^{(1)} \cdot \dot{\mathbf{S}})$ vanishes and, according to Eq. (22), the spin-galvanic effect is not contributed by the relaxational mechanism and arises only due to the kinetic mechanism described by Eq. (21). The observation of the Hanle effect, see Fig. 7, demonstrates that free carrier intrasubband transitions can polarize the spins of electron systems. The measurements allow one to extract the spin relaxation time τ_s from the peak position of the photocurrent reached at $\omega_L \tau_s = 1$ providing experimental access to investigation of spin relaxation times for monopolar spin orientation, where only one type of charge carriers is involved in the excitation-relaxation process [41, 48]. This condition is close to that of electrical spin injection in semiconductors.

We note that a similar set-up was applied in experiments of Bakun et al. [49] carried out on bulk AlGaAs excited by interband absorption and demonstrating spin photocurrents caused by the inhomogeneous spin distribution predicted in [50, 51], known now as the Inverse Spin Hall Effect. The crucial difference to the spin-galvanic effect is that in the case of surface photocurrent caused by optical orientation a gradient of spin density is needed. Naturally this gradient is absent in QWs where the spin-galvanic effect has been investigated because QWs are two-dimensional and have no “thickness”.

For optical excitation of the spin-galvanic effect mid-infrared, far-infrared (terahertz frequencies) and visible laser radiation has been used [2, 10, 11]. Most of the measurements were carried out in the long wavelength range with photon energies less than the energy gap of investigated semiconductors. The advantage is that, in contrast to interband excitation resulting in the valence band – conduction band transitions, there are no spurious photocurrents due to other mechanisms like the Dember effect, photovoltaic effects at contacts and Schottky barriers etc.

In contrast to the circular PGE the spin-galvanic effect induced by the Hanle effect under intersubband transitions excited by the mid-infrared radiation does

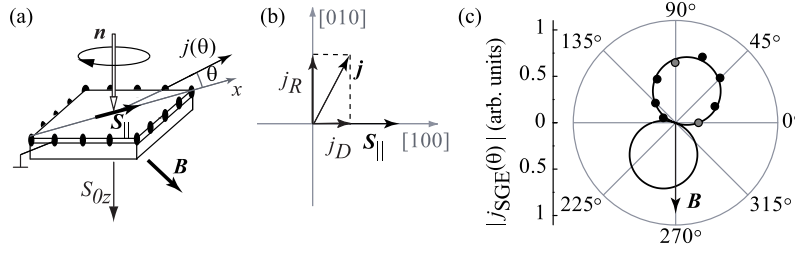


FIG. 8: The separation of the SIA and BIA contributions to the spin-galvanic effect observed in an n -type InAs single QW at room temperature for the case of the electron spin $\mathbf{S}_{\parallel} \parallel [100]$. (a) Geometry of the experiment. (b) The direction of the SIA and BIA contributions to the photocurrent. (c) The spin galvanic current measured as a function of the angle ϑ between the pair of contacts and the x axis. After [53].

not change its sign with frequency radiation and follows the spectral behavior of direct intersubband absorption [48]. This result is in agreement with the mechanism of the spin-galvanic effect discussed in the previous subsection, see Eqs. (23), and clearly demonstrates that this effect has different microscopic origin. The observation of the mid-infrared and terahertz radiation excited spin-galvanic effect, which is due to spin orientation, gives clear evidence that direct intersubband and Drude absorption of circularly polarized radiation result in a monopolar spin orientation. Mechanisms of the monopolar spin orientation were analyzed in Refs. [48, 52]. We would like to emphasize that spin-sensitive $e1-e2$ intersubband transitions in (001)-grown n -type QWs have been observed at normal incidence when there is no component of the electric field of the radiation normal to the plane of the QWs.

C. Spin-Galvanic Effect at Zero Magnetic Field

In the experiments described above an external magnetic field was used for re-orientation of an optically generated spin polarization. The spin-galvanic effect can also be generated at optical excitation only, without application of an external magnetic field. The necessary in-plane component of the spin polarization can be obtained by oblique incidence of the exciting circularly polarized radiation but in this case the circular PGE may also occur interfering with the spin-galvanic effect. However, the spin-galvanic effect due to pure optical excitation was demonstrated making use the difference in spectral behavior of these two effects excited by inter-subband transitions in n -type GaAs QWs [43]. Experiments have been carried out making use of the spectral tunability of the free electron laser “FELIX”. The helicity dependent photocurrent closely following the absorption spectrum was detected demonstrating dominant contribution of the spin-galvanic effect.

D. Determination of the SIA/BIA Spin Splitting Ratio

An important application of the spin-galvanics was addressed in [53]. It was demonstrated that angular dependent measurements of spin photocurrents allow one to separate the different contributions to the spin-orbit Hamiltonian (9). Later on this method was extended and improved by using measurements of both the spin-galvanic effect (at normal incidence of the radiation in the presence of an in-plane magnetic field) and circular PGE (at oblique incidence with no magnetic field applied) [24, 54].

Experiments were carried out on (001)-oriented QWs for which the Hamiltonian Eq. (9) for the first subband reduces to

$$\mathcal{H}_{\mathbf{k}}^{(1)} = \alpha(\sigma_{x_0} k_{y_0} - \sigma_{y_0} k_{x_0}) + \beta(\sigma_{x_0} k_{x_0} - \sigma_{y_0} k_{y_0}), \quad (25)$$

where x_0, y_0 are the crystallographic axes [100] and [010], the parameters α and β result from the structure-inversion and bulk-inversion asymmetries, SIA and BIA, respectively. The first and second contributions to the Hamiltonian (25) are often called the Rashba and Dresselhaus terms.

Note that, in the coordinate system with $x \parallel [1\bar{1}0]$ and $y \parallel [110]$, the matrix $\mathcal{H}_{\mathbf{k}}^{(1)}$ gets the form $\beta_{xy}\sigma_x k_y + \beta_{yx}\sigma_y k_x$ with $\beta_{xy} = \beta + \alpha$, $\beta_{yx} = \beta - \alpha$. According to Eq. (21) the current components j_x, j_y are proportional, respectively, to β_{xy} and β_{yx} and, therefore, angular dependent measurements of spin photocurrents allow one to separate the SIA and BIA linear in- \mathbf{k} terms. By mapping the magnitude of the spin photocurrent in the QW plane the ratio of both terms can directly be determined from experiment and does not rely on theoretically obtained quantities. The relation between the photocurrent and spin directions can be conveniently expressed in the following matrix form

$$\mathbf{j} \propto \begin{pmatrix} \beta & -\alpha \\ \alpha & -\beta \end{pmatrix} \mathbf{S}_{\parallel}, \quad (26)$$

where \mathbf{j} and \mathbf{S}_{\parallel} are two-component columns with the in-plane components along the crystallographic axes $x_0 \parallel$

[100] and $y_0 \parallel [010]$. The directions of the SIA and BIA coupling induced photocurrents are shown in Fig. 8(b) for the particular case $\mathbf{S}_{\parallel} \parallel [100]$.

Figure 8(c) shows the angular dependence of the spin-galvanic current $j(\vartheta)$ measured on an n -type (001)-grown InAs/Al_{0.3}Ga_{0.7}Sb single QW of 15 nm width at room temperature. Because of the admixture of photon helicity-independent magneto-gyrotropic effects (see Section VB1) the spin-galvanic effect is extracted after eliminating current contributions which are helicity-independent: $j = (j_{\sigma_+} - j_{\sigma_-})/2$.

The sample edges are oriented along the $[1\bar{1}0]$ and $[110]$ crystallographic axes. Eight pairs of contacts on the sample allow one to probe the photocurrent in different directions, see Fig. 8(a). The optical spin orientation was performed by using a pulsed molecular NH₃ laser. The photocurrent \mathbf{j} is measured in the unbiased structure in a closed circuit configuration. The nonequilibrium in-plane spin polarization \mathbf{S}_{\parallel} is prepared as described in Section III B, see also Fig. 8(a). The angle between the magnetic field and \mathbf{S}_{\parallel} can in general depend on details of the spin relaxation process. In these particular InAs QW structures the isotropic Elliott–Yafet spin relaxation mechanism dominates. Thus, the in-plane spin polarization \mathbf{S}_{\parallel} is always perpendicular to \mathbf{B} and can be varied by rotating \mathbf{B} around z as illustrated in Fig. 8(a). The circle in Fig. 8(c) represents the angular dependence $\cos(\vartheta - \vartheta_{\max})$, where ϑ is the angle between the pair of contacts and the x axis and $\vartheta_{\max} = \arctan(j_R/j_D)$, with j_R and j_D being the SIA and BIA contributions to the photocurrent, respectively. The best fit in this sample is achieved for the ratio $j_R/j_D = \alpha/\beta = 2.1$. The method was also used for investigation of SIA/BIA \mathbf{k} -linear spin-splitting in GaAs heterostructures where spin relaxation is controlled by Dyakonov–Perel mechanism [54]. These experiments demonstrate that growth of structures with various delta-doping layer position accompanied by experiments on spin-galvanic effect makes possible a controllable variation of the structure inversion asymmetry and preparation of samples with equal SIA and BIA constants or with a zero SIA constant.

The measurements of the spin-galvanic and circular photogalvanic effects in a set of InGaAs/InAlAs QW structures with semitransparent gate, supported by the weak antilocalization experiments, permitted to find a proper QW design for the realization of the persistent helix condition $|\alpha| = |\beta|$ of the parameters in Eq. (25) [55]. Application of the two complementary experiments, transport and photogalvanic, enabled to extract information on the role of cubic-in- \mathbf{k} terms on spin transport in a material with strong spin-orbit interaction, for details see the review [24].

E. Coherent Trembling Motion of Spin-Polarized Electrons

Equation (22) is derived for the steady-state spin generation. If the electron spin \mathbf{S} varies in time then this equation reads

$$\mathbf{j} = en_s\tau_p\nabla_{\mathbf{k}} \left[\boldsymbol{\Omega}_{\mathbf{k}}^{(1)} \left(-\dot{\mathbf{S}} + \frac{d\mathbf{S}(t)}{dt} \right) \right]. \quad (27)$$

Particularly, under a short-pulse interband excitation at $t = 0$ by circularly polarized light, the spin-galvanic current at $t > 0$ has the form

$$\mathbf{j} = en_s\tau_p\nabla_{\mathbf{k}} \left(\boldsymbol{\Omega}_{\mathbf{k}}^{(1)} \frac{d\mathbf{S}(t)}{dt} \right). \quad (28)$$

In the normal-incidence geometry and in the presence of an in-plane magnetic field $\mathbf{B} \parallel x$ the electron spin $\mathbf{S}(t)$ precesses around the field and exhibits an oscillatory behaviour

$$\begin{aligned} S_z(t) &= S_z(0)e^{-t/\tau_s} \cos(\omega_L t), \\ S_y(t) &= -S_z(0)e^{-t/\tau_s} \sin(\omega_L t). \end{aligned} \quad (29)$$

Substituting $S_y(t)$ into Eq. (28) we find for the x -component of the electric current

$$\begin{aligned} j_x(t) &= 2en_s\tau_p \frac{\beta_{yx}}{\hbar} S_z(0)e^{-t/\tau_s} \\ &\times \left[\frac{1}{\tau_s} \sin(\omega_L t) - \omega_L \cos(\omega_L t) \right]. \end{aligned} \quad (30)$$

Stepanov et al. [56] have measured under identical experimental conditions the time-resolved spin-Faraday rotation of electron spin precession $S_z(t)$ and time-dependent ac difference current $j_{\text{spin}} = [j(\sigma_+) - j(\sigma_-)]/2$ induced by the pump pulses with σ_+/σ_- helicities. The samples consisted of a 500 nm thick In_{0.07}Ga_{0.93}As epilayer grown on a semi-insulating (001) GaAs wafer. Due to the strain caused by the lattice mismatch and the reduced symmetry of the structure, the spin-orbit terms in the electron effective Hamiltonian have the form similar to Eq. (25). A series of the current measurements at different values of the magnetic field are shown in Fig. 9(a). The current can be fitted by an exponentially decaying cosine function

$$j_x(t) = j_0 e^{-t/\tau_s} \cos(\omega_L t + \phi),$$

with the amplitude

$$j_0 \propto \beta_{yx} S_z(0) \text{sign}(B_x) \sqrt{\omega_L^2 + \tau_p^{-2}} \quad (31)$$

and the phase $\phi = -\cot^{-1}(\omega\tau_s)$. Figure 9(b) presents the experimental and calculated dependences of the amplitude j_0 on the magnetic field.

The ac current (30) can be understood in terms of the coherent trembling motion (Zitterbewegung) of spin-polarized electrons [56]. The trembling motion originates

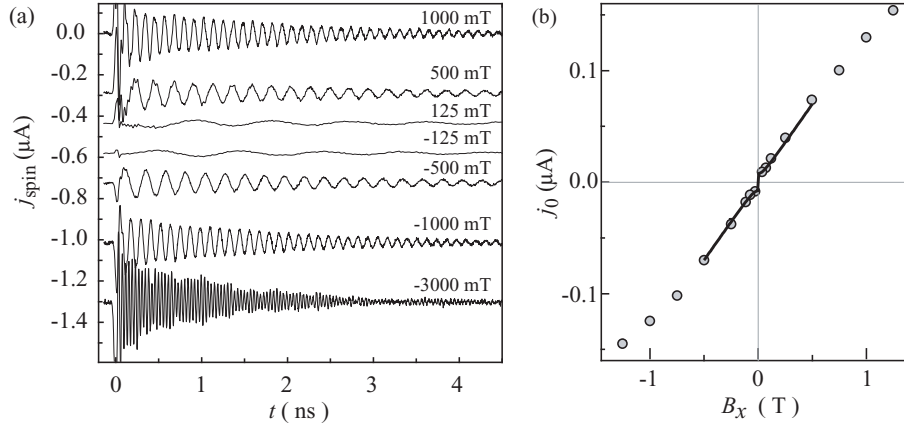


FIG. 9: Magnetic field dependence of spin precession driven coherent Zitterbewegung. (a) Time-resolved ac current along the $[110]$ direction in the InGaAs(001) epilayer at various magnetic fields. Larmor precession frequency and magnitude of ac current increase with increasing magnetic field strength while the sign of the ac current reverses when reversing the magnetic field direction. (b) Amplitude j_0 of ac current vs. applied magnetic field B_x . The solid line is a fit to Eq. (31). After [56].

from the fact that, in quantum mechanics, the electron velocity is not a conserved quantity in the presence of spin-orbit interaction. Taking into account the linear in \mathbf{k} terms (9) and the Zeeman Hamiltonian $(\hbar/2)\omega_L\sigma_x$ we have for the electron velocity $v_x = (\hbar k_x/m_c) + (\beta_{yx}/\hbar)\sigma_y$ and then obtain for the acceleration

$$\frac{dv_x}{dt} = -\frac{\beta_{yx}}{\hbar}\omega_L\sigma_z.$$

Including the electron momentum scattering as a “friction force” and neglecting the spin relaxation we arrive at the following equation for the average electron velocity

$$\frac{dv_x}{dt} + \frac{v_x}{\tau_p} = -\frac{2\beta_{yx}}{\hbar}\omega_L S_z.$$

In the fast scattering limit, $\omega_L\tau_p \ll 1$, the oscillating current is given by

$$j_x = en_s v_x(t) = -2n_s\tau_p \frac{\beta_{yx}}{\hbar}\omega_L S_z(0) \cos(\omega_L t), \quad (32)$$

in agreement with Eq. (30) where τ_s is set to infinity.

IV. INVERSE SPIN-GALVANIC EFFECT

The effect inverse to the spin-galvanic effect is the electron spin polarization generated by a charge current \mathbf{j} . First it was predicted in [4] and observed in bulk tellurium [57], see also the recent paper [58]. The symmetry of bulk tellurium belongs to the gyrotropic crystal class D_3 which contains the right or left handed three-fold screw axis, respectively the space groups D_3^4 and D_3^6 . The extrema of the conduction and valence are located at the vortices of the hexagonal Brillouin zone, the points H and H' (M and P in other notation). The degeneracy in the valence band is completely lifted, the two upper nondegenerate subbands H_4 and H_5 are split by

$2\Delta = 126$ meV. The hole wave function in the subband H_4 is a superposition of the two Bloch states $|\pm 3/2\rangle$

$$\Psi_{H_4, k_z} = C_{\frac{3}{2}}(k_z)|3/2\rangle + C_{-\frac{3}{2}}(k_z)|-3/2\rangle,$$

where

$$C_{\pm\frac{3}{2}}(k_z) = \sqrt{\frac{E \pm \beta k_z}{2E}}, \quad E = \sqrt{\Delta^2 + (\beta k_z)^2},$$

and the spin-orbit coefficient $\beta = 2.4 \times 10^{-8}$ eV·cm. The average component of the angular momentum on the principal axis z is given by

$$S_z(k_z) = \frac{1}{2} \left(C_{\frac{3}{2}}^2 - C_{-\frac{3}{2}}^2 \right) = \frac{\beta k_z}{2E}. \quad (33)$$

An external cw electric field \mathbf{F} applied in the z direction shifts the hole distribution in the \mathbf{k} -space by the drift wave vector $\bar{k}_z \propto F_z$ and induces the free-carrier spin $S_z \approx \beta \bar{k}_z / 2\Delta$. The appearance of the current-induced spin induces the rotation of the polarization plane of the linearly polarized probe light [57, 58] and the circular polarization of the interband photoluminescence.

In p -type tellurium, the energy splitting between the nondegenerate valence subbands H_4 and H_5 exceeds the uncertainty \hbar/τ_p , the spin \mathbf{S} and the wave vector \mathbf{k} are strictly coupled, and the off-diagonal intersubband components of the hole density matrix are negligible. In the opposite limiting case where the splitting of the conduction band due to the linear \mathbf{k} terms (9) is small as compared to \hbar/τ_p , the off-diagonal components of the electron spin density matrix $\rho_{\mathbf{k}}$ are not suppressed by the splitting and the relation between the nonequilibrium spin and the wave vector is more loose. The spin orientation by current in this limit of fast momentum scattering was theoretically demonstrated for QW systems by Vas'ko and Prima [59], Levitov et al. [60], Aronov and Lyanda-Geller [61] and Edelstein [62]. The study

was extended in Refs. [63–72], see the review [3] for more details. The first direct experimental proofs of this effect were obtained in semiconductor QWs [73, 74] as well as in strained bulk material [75]. At present inverse spin-galvanic effect has been observed in various low-dimensional structures based on GaAs, InAs, ZnSe and GaN.

Phenomenologically, the averaged nonequilibrium free-carrier spin \mathbf{S} is linked to \mathbf{j} by Eq. (3). Microscopically, the spin polarization can be found from the kinetic equation for the electron spin density matrix $\rho_{\mathbf{k}}$ which can conveniently be presented in the form

$$\rho_{\mathbf{k}} = f_{\mathbf{k}} + \mathbf{s}_{\mathbf{k}} \boldsymbol{\sigma}, \quad (34)$$

where $f_{\mathbf{k}} = \text{Tr}\{\rho_{\mathbf{k}}/2\}$ is the distribution function and $\mathbf{s}_{\mathbf{k}} = \text{Tr}\{\rho_{\mathbf{k}}\boldsymbol{\sigma}/2\}$ is the average spin in the \mathbf{k} state. In the presence of an electric field \mathbf{F} the kinetic equation reads

$$\frac{e\mathbf{F}}{\hbar} \frac{\partial \rho_{\mathbf{k}}}{\partial \mathbf{k}} + \frac{i}{\hbar} [\mathcal{H}_{\mathbf{k}}^{(1)}, \rho_{\mathbf{k}}] + Q_{\mathbf{k}}\{\rho\} = 0, \quad (35)$$

where $Q_{\mathbf{k}}\{\rho\}$ is the collision integral and $\mathcal{H}_{\mathbf{k}}^{(1)}$ is the linear- \mathbf{k} Hamiltonian. Similarly to the spin-galvanic effect there exist two different mechanisms of the current-to-spin transformation, namely, spin-flip mediated and precessional.

A. Spin-Flip Mediated Current-Induced Polarization

In the spin-flip mediated mechanism, a value of the spin generation rate is calculated neglecting the commutator in Eq. (35) and taking into account the spin-flip processes in the collision integral and the linear- \mathbf{k} terms in the electron dispersion. Microscopic illustration of this mechanism is sketched in Fig. 10(b) for a 2D hole gas in a system of the C_s symmetry, a situation relevant for the experiments of Ref. [73].

In the simplest case the electron kinetic energy in a QW depends quadratically on the in-plane wave vector \mathbf{k} . In equilibrium, the spin degenerate \mathbf{k} states are symmetrically occupied up to the Fermi energy E_F . If an external electric field is applied, the charge carriers drift in the direction of the resulting force. The carriers are accelerated by the electric field and gain kinetic energy until they are scattered, Fig. 10(a). A stationary state forms where the energy gain and the relaxation are balanced resulting in an asymmetric distribution of carriers in the \mathbf{k} -space. The holes acquire the average quasi-momentum

$$\hbar \bar{\mathbf{k}} = -e\tau_p \mathbf{F} = -\frac{m_c}{en_s} \mathbf{j}, \quad (36)$$

where τ_p is the momentum relaxation time, \mathbf{j} the electric current density, m_c the effective mass and n_s the 2D carrier concentration. As long as the energy band is spin degenerated in the \mathbf{k} -space a current is not accompanied

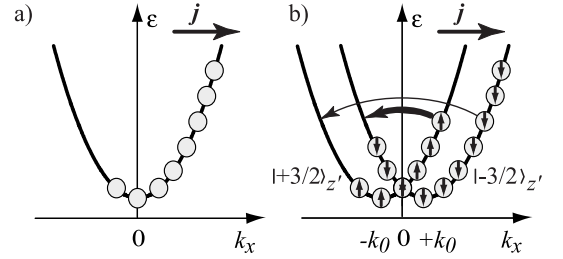


FIG. 10: Comparison of current flow in (a) spin-degenerate and (b) spin-split subbands. (a) Hole distribution at a stationary current flow due to acceleration in an electric field and momentum relaxation. (b) Spin polarization due to spin-flip scattering. Here only $\beta_{z'x}\sigma_{z'}k_x$ term is taken into account in the Hamiltonian which splits the valence subband into two parabolas with spin-up $|+3/2\rangle_{z'}$ and spin-down $|-3/2\rangle_{z'}$ in the z' -direction. Biasing along the x -direction causes an asymmetric in \mathbf{k} -space occupation of both parabolas. After [73].

by spin orientation. However, in zinc-blende-lattice QWs or strained bulk semiconductors the spin degeneracy is lifted due to the linear- \mathbf{k} terms given by Eq. (9). To be specific for the mechanism depicted in Fig. 10(b) we consider solely spin-orbit interaction of the form $\beta_{z'x}\sigma_{z'}k_x$. Then the parabolic energy band splits into two parabolic subbands of opposite spin directions, $s_{z'} = 3/2$ and $s_{z'} = -3/2$, with minima symmetrically shifted in the \mathbf{k} -space along the k_x axis from the point $k = 0$ into the points $\pm k_0$, where $k_0 = m_c\beta_{z'x}/\hbar^2$. The corresponding dispersion is sketched in Fig. 10(b).

In the presence of an in-plane electric field $\mathbf{F} \parallel x$ the distribution of carriers in the \mathbf{k} -space gets shifted yielding an electric current. Until the spin relaxation is switched off the spin branches are equally populated and equally contribute to the current. Due to the band splitting, spin-flip relaxation processes $\pm 3/2 \rightarrow \mp 3/2$ are different because of the difference in quasi-momentum transfer from initial to final states. In Fig. 10(b) the \mathbf{k} -dependent spin-flip scattering processes are indicated by arrows of different lengths and thicknesses. As a consequence different amounts of spin-up and spin-down carriers contribute to the spin-flip transitions causing a stationary spin orientation. Thus, in this picture we assume that the origin of the current induced spin orientation is, as sketched in Fig. 10(b), exclusively due to scattering and hence dominated by the Elliott-Yafet spin relaxation processes.

B. Precessional Mechanism

The precessional mechanism resulting in the current induced spin orientation is based on the Dyakonov–Perel spin relaxation. In this mechanism of spin polarization the contribution of spin-flip scattering to the collision integral is ignored and the spin appears taking into account the linear- \mathbf{k} Hamiltonian, both in the collision integral

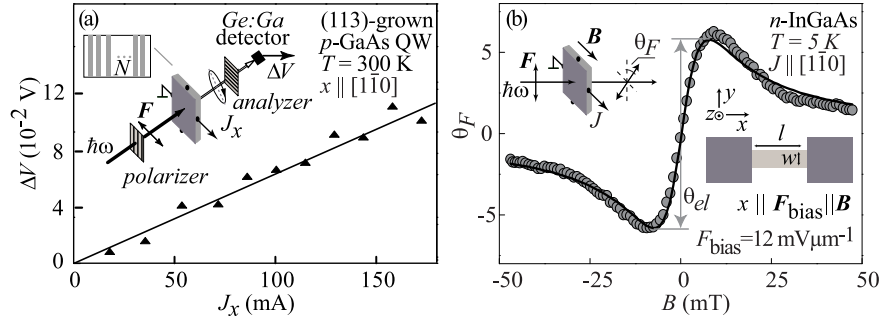


FIG. 11: (a) Polarization dependent signal for current in the active direction as a function of current strength for two samples. After Ref. [73]. (b) Voltage-induced angle θ_F as a function of the magnetic field B for $F = 12 \text{ mV } \mu\text{m}^{-1}$ ($\mathbf{F} \parallel [1\bar{1}0]$). After Ref. [75]. Open circles are data, and lines are fits according Eq. (41). Insets to both panels show experimental set-up: (a) The sample is placed between crossed polarizer and analyzer blocking optical transmission at zero current through the sample. Injecting a modulated current in the sample yields a signal at the detector which is recorded by the box-car technique. (b) The current yields an in-plane spin polarization which applying magnetic field B is rotated out off plane yielding Faraday rotation of the probe light. Second inset shows sample geometry. Here dark areas are Ni/GeAu contacts and the light grey area is the InGaAs channel.

and the commutator $[\mathcal{H}_{\mathbf{k}}^{(1)}, \rho_{\mathbf{k}}]$. For example, we present here the collision integral for elastic scattering

$$Q_{\mathbf{k}}\{\rho\} = \frac{2\pi}{\hbar} N_i \sum_{\mathbf{k}'} |A_{\mathbf{k}'\mathbf{k}}|^2 \times \left\{ \delta \left(E_{\mathbf{k}} + \mathcal{H}_{\mathbf{k}}^{(1)} - E_{\mathbf{k}'} - \mathcal{H}_{\mathbf{k}'}^{(1)} \right), \rho_{\mathbf{k}} - \rho_{\mathbf{k}'} \right\}, \quad (37)$$

where $E_{\mathbf{k}} = \hbar^2 k^2 / (2m_c)$, N_i is the density of static defects acting as the scatterers, $A_{\mathbf{k}'\mathbf{k}}$ is the scattering matrix element and the braces mean the anticommutator, $\{AB\} = (AB + BA)/2$ for two arbitrary 2×2 matrices A and B . Similar equation can be written for electron-phonon scattering.

In the equilibrium the electron spin density matrix is given by

$$\rho_{\mathbf{k}}^0 = f^0(E_{\mathbf{k}} + \mathcal{H}_{\mathbf{k}}^{(1)}) \approx f^0(E_{\mathbf{k}}) + \frac{\partial f^0}{\partial E_{\mathbf{k}}} \mathcal{H}_{\mathbf{k}}^{(1)}, \quad (38)$$

where $f^0(E) = \{\exp[(E - \mu)/k_B T] + 1\}^{-1}$ is the Fermi-Dirac distribution function, μ is the electron chemical potential, k_B is the Boltzmann constant and T is the temperature.

Neglecting the spin splitting we can write the solution of Eq. (35) in the text-book form

$$f_{\mathbf{k}} = f^0(E_{\mathbf{k}}) - eF_x v_x \tau_1(E_{\mathbf{k}}) \frac{\partial f^0}{\partial E_{\mathbf{k}}} \quad (39)$$

with $\mathbf{s}_{\mathbf{k}} = 0$. Here $v_x = \hbar k_x / m_c$, τ_1 is the time describing the relaxation of a distribution-function harmonic with the angular dependence of the functions k_x or k_y . If we substitute $\rho_{\mathbf{k}}$ with the distribution function (39) into the collision integral and $\rho_{\mathbf{k}}^0$ into the first term of Eq. (35) we obtain an equation for $\mathbf{s}_{\mathbf{k}}$. By solving this equation one arrives at the estimation for the spin density

$$s_{\mu} \equiv \sum_{\mathbf{k}} s_{\mathbf{k},\mu} \sim \beta_{\mu\lambda} \bar{k}_{\lambda} g_{2d}, \quad (40)$$

where $g_{2d} = m_c / (\pi \hbar^2)$ is the 2D density of states and $\hbar \bar{k}_{\lambda} / m_c$ is the electron drift velocity. The factor of proportionality can be found in [65, 68, 70–72].

Spin orientation by electric current in low-dimensional structures has been observed applying various experimental techniques, comprising transmission of polarized THz-radiation, polarized luminescence and space resolved Faraday rotation [27, 73–80]. Here we briefly sketch results of experiments on the THz-transmission and polarized photoluminescence in which the spin orientation by electric current in QW structures was initially observed.

It has been shown that in the streaming regime the current-induced spin orientation is remarkably increased [81]. A microscopic theory of spin orientation by electric current for the hopping regime has been developed by Smirnov and Golub [82].

C. Current Induced Spin Faraday Rotation

In order to observe current induced spin polarization, in [73] the circular dichroism and Faraday rotation of THz radiation transmitted through samples containing multiple QWs were studied. This method allows one to detect spin polarization at normal incidence in the growth direction. The materials chosen for studies were (113)- and miscut (001)-oriented p -type GaAs multiple QWs of the C_s point group symmetry. The transmission measurements were carried out at room temperature using linearly polarized $\lambda = 118 \mu\text{m}$ radiation as shown in Fig. 11(a): the sample is placed between two metallic grid polarizers and the cw -terahertz radiation is passed through this optical arrangement.

Using modulation technique the Faraday rotation was observed only for the current flowing in the x -direction. This is in agreement with the phenomenological equation $S_{z'} = R_{z'x} j_x$ relating the induced spin with the current

density, the spin polarization can be obtained only for the current flowing along the direction normal to the mirror reflection plane which is perpendicular to the x -axis. The signal ΔV caused by rotation of polarization plane is shown in Fig. 11(a) as a function of the current strength. Experiment shows that, in agreement with Eq. (40), the spin polarization increases with the decreasing temperature.

Current induced spin polarization has also been detected by the Faraday rotation of infrared radiation applying a mode-locked Ti:sapphire laser. Figure 11(b) demonstrates an optical detection of current-induced electron spin polarization in strained InGaAs epitaxial layers [75]. The heterostructure studied consists of 500 nm of n -In_{0.07}Ga_{0.93}As (Si doped for $n = 3 \times 10^{16} \text{ cm}^{-3}$) grown on (001) semiinsulating GaAs substrate and capped with 100 nm of undoped GaAs. The n -InGaAs layer is strained due to the lattice mismatch. An alternating electric field \mathbf{F} is applied along either of the two crystal directions $[110]$ and $[\bar{1}\bar{1}0]$, the in-plane magnetic field \mathbf{B} is parallel to \mathbf{F} . A linearly polarized probe beam is directed along the z axis, normally incident and focused on the sample. The polarization axis of the transmitted beam rotates by an angle θ_F that is proportional to the z component of the spins S_z (the spin Faraday rotation).

The current-induced angle is lock-in detected at the modulation frequency as a function of the applied magnetic field. The experiment data in Fig. 11(b) can be explained by assuming a constant orientation rate $\dot{s}_{\mathbf{k},y}$ for spins polarized along the y axis. The rotation of the spins around the magnetic field yields the z spin component given by

$$S_z(B) = \frac{\omega_L \tau_{s\parallel}}{1 + (\omega_L \tau_s)^2} S_{0y}, \quad S_{0y} = \tau_{s,\perp} \sum_{\mathbf{k}} \frac{\dot{s}_{\mathbf{k},y}}{n_s}, \quad (41)$$

where the notations for the spin relaxation times and Larmor frequency are introduced in Eq. (24). The high sensitivity of the Faraday rotation technique allows detection of 100 spins in an integration time of about 1 s, unambiguously revealing the presence of a small spin polarization due to laterally applied electric fields.

D. Current Induced Polarization of Photoluminescence

In [74, 76] in order to detect the inverse spin-galvanic effect the degree of circular polarization of the 2D hole gas photoluminescence (PL) was measured. This experimental procedure has become a proven method for probing spin polarization [1, 83]. A (001)-grown sample cleaved into bars was studied with the current flowing along the long side cleaved parallel to the $[\bar{1}\bar{1}0]$ direction. Lately (113)-grown samples were also studied [76]. The PL was excited with 633 nm line from a helium-neon laser. In (001)-oriented samples the PL was collected from the cleaved (110) facet of the sample.

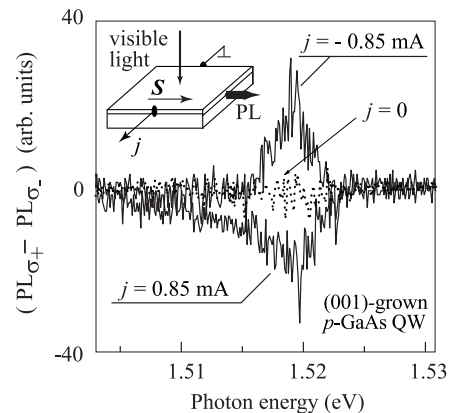


FIG. 12: Differential spectra of polarized PL for two current directions. After [74]. Base line is taken with the current turned off. Inset shows experimental geometry.

On the other hand, at the (113)-oriented heterojunctions, because of the C_s symmetry, the mean spin density will have a component along the growth direction. Therefore, the PL in this case was detected in the back scattering geometry; the degree of PL circular polarization P_c was analyzed with a $\lambda/4$ plate and a linear polarizer. Inset in Fig. 12 shows the experimental arrangement for measuring the current induced polarization and differential spectra, $(PL_{\sigma_+} - PL_{\sigma_-})$, for the two opposite current directions. The observation of the circularly polarized radiation and, in particular, the reversal of helicity upon the inversion of the current direction demonstrate the effect of current induced spin polarization. The observed degree of polarization in (001)-grown samples yields a maximum of 2.5% [74]. In (113)-grown samples even higher polarization of 12% at 5.1 K is achieved [76].

V. PURE SPIN CURRENTS

Pure spin current represents a nonequilibrium distribution where free carriers, electrons or holes, with the spin up propagate mainly in one direction and an equal number of spin-down carriers propagates in the opposite direction. This state is characterized by zero charge current because electric currents contributed by spin-up and spin-down quasi-particles cancel each other, but leads to separation of spin-up and spin-down electron spatial distributions and accumulation of the opposite spins at the opposite edges of the sample. Spin currents in semiconductors can be driven by an electric field acting on unpolarized free carriers (the spin Hall effect, not considered here). They can be induced as well by optical means under interband or intraband optical transitions in non-centrosymmetric bulk and low-dimensional semiconductors [84–89].

A. Pure Spin Current Injected by a Linearly Polarized Beam

In general, the spin current density pseudotensor $q_{\lambda\mu}$ describes the flow of the μ component of the spin polarization in the spatial direction λ . Phenomenologically, the spin photocurrent $q_{\lambda\mu}$ is related with bilinear products $Ie_\nu e_\eta^*$ by a fourth-rank tensor, in Eq. (4) it is the tensor $P_{\lambda\mu\nu\eta}$. Here we assume the light to be linearly polarized. In this particular case the product $e_\nu e_\eta^* \equiv e_\nu e_\eta$ is real and the tensor $P_{\lambda\mu\nu\eta}$ is symmetric with respect to interchange of the third and fourth indices.

Among microscopic mechanisms of the pure spin photocurrent we first discuss those related to the \mathbf{k} -linear terms in the electron effective Hamiltonian [85, 87]. Let us consider the $e1$ - $hh1$ interband absorption of linearly polarized light under normal incidence on (001)-grown QWs. In this case linear- \mathbf{k} splitting of the $hh1$ heavy-hole valence subband is negligibly small. For the sake of simplicity, but not at the expense of generality, in the $e1$ conduction subband we take into account the spin-orbit term $\beta_{yx}\sigma_y k_x$ only, the contribution to the tensor \mathbf{P} coming from the term $\beta_{xy}\sigma_x k_y$ is considered similarly. Then the conduction-electron spin states are eigen states of the spin matrix σ_y . For the light linearly polarized, say, along x , all the four transitions from each heavy-hole state $\pm 3/2$ to each $s_y = \pm 1/2$ state are allowed. The energy and momentum conservation laws read

$$E_g^{\text{QW}} + \frac{\hbar^2(k_x^2 + k_y^2)}{2\mu_{cv}} + 2s_y\beta_{yx}k_x = \hbar\omega,$$

where we use the same notations for E_g^{QW} and μ_{cv} as in Subsection III F. For a fixed value of k_y the photoelectrons are generated only at two values of k_x labeled k_x^\pm . The average electron velocity in the s_y spin subband is given by

$$\bar{v}_{e,x} = \frac{\hbar(k_x^+ + k_x^-)}{2m_c} + 2s_y \frac{\beta_{yx}}{\hbar} = \frac{2s_y\beta_{yx}}{\hbar} \frac{m_c}{m_c + m_v}.$$

The resulting spin fluxes $\mathbf{i}_{\pm 1/2}$ are opposite in sign, the electric current $\mathbf{j} = e(\mathbf{i}_{1/2} + \mathbf{i}_{-1/2})$ is absent but the spin current $\mathbf{j}_s = (\mathbf{i}_{1/2} - \mathbf{i}_{-1/2})/2$ is nonzero. This directional movement decays in each spin subband within the momentum relaxation time τ_p^e . However under the cw photoexcitation the electron generation is continuous which results in the spin current

$$q_{xy} = \frac{\beta_{yx}\tau_p^e}{2\hbar} \frac{m_c}{m_c + m_v} \frac{\eta_{eh}I}{\hbar\omega}.$$

Under the normal incidence it is independent of the light polarization plane.

Now we turn to the pure spin currents excited in (110)-grown QWs. In these structures the spin component along the normal z' || [110] is coupled with the in-plane electron wave vector \mathbf{k} || [1 $\bar{1}$ 0] due to the term $\beta_{z'x}\sigma_{z'}k_x$ in the conduction band and the term proportional to

$J_{z'}k_x$ in the heavy-hole band where $J_{z'}$ is the 4×4 matrix of the angular momentum $3/2$. The coefficient $\beta_{z'x}^{(e1)}$ is relativistic and can be ignored compared with the non-relativistic constant $\beta_{z'x}^{(hh1)}$ describing the spin splitting of heavy-hole states. The allowed direct optical transitions from the valence subband $hh1$ to the conduction subband $e1$ are $|+3/2\rangle \rightarrow |+1/2\rangle$ and $|-3/2\rangle \rightarrow |-1/2\rangle$, where $\pm 1/2, \pm 3/2$ indicate the z' components of the electron spin and hole angular momentum. Under linearly polarized photoexcitation the charge photocurrent is not induced, and for the electron pure spin photocurrent one has

$$q_{xz'} = \frac{\beta_{z'x}^{(hh1)}\tau_p^e}{2\hbar} \frac{m_v}{m_c + m_v} \frac{\eta_{eh}I}{\hbar\omega}. \quad (42)$$

The similar hole spin current can be ignored in the spin separation experiments because of the much shorter spin relaxation time for holes as compared to the conduction electrons.

Another contribution to spin photocurrents comes from \mathbf{k} -linear terms in the matrix elements of the interband optical transitions [90]. Taking into account $\mathbf{k} \cdot \mathbf{p}$ admixture of the remote Γ_{15} conduction band to the Γ_{15} valence-band states $X_0(\mathbf{k}), Y_0(\mathbf{k}), Z_0(\mathbf{k})$ and the Γ_1 conduction-band states $S(\mathbf{k})$, one derives the interband matrix elements of the momentum operator for bulk zincblende-lattice semiconductors [91, 92]

$$\langle iS(\mathbf{k}) | \mathbf{e} \cdot \mathbf{p} | X_0(\mathbf{k}) \rangle = \mathcal{P}[e_{x_0} + i\chi(e_{y_0}k_{z_0} + e_{z_0}k_{y_0})], \quad (43)$$

$\langle iS(\mathbf{k}) | \mathbf{e} \cdot \mathbf{p} | Y_0(\mathbf{k}) \rangle$ and $\langle iS(\mathbf{k}) | \mathbf{e} \cdot \mathbf{p} | Z_0(\mathbf{k}) \rangle$ are obtained by the cyclic permutation of indices, the coefficient χ is a material parameter dependent on the interband spacings and interband matrix elements of the momentum operator at the Γ point, and we use here the crystallographic axes $x_0 \parallel [100]$ etc. For GaAs band parameters [93] the coefficient χ can be estimated as 0.2 \AA .

Calculation for (110)-grown QWs shows that the spin photocurrent caused by \mathbf{k} -linear terms in the interband matrix elements has the form

$$q_{xz'} = \varepsilon(e_{y'}^2 - e_{x'}^2) \frac{\chi\tau_p^e}{\hbar} \frac{\eta_{cv}}{\hbar\omega} I, \quad (44)$$

$$q_{y'z'} = \varepsilon e_x e_{y'} \frac{\chi\tau_p^e}{\hbar} \frac{\eta_{ev}}{\hbar\omega} I$$

with $\varepsilon = (\hbar\omega - E_g^{\text{QW}})m_v/(m_c + m_v)$ being the kinetic energy of the photoexcited electrons and $y' \parallel [00\bar{1}]$. In contrast to Eq. (42), this contribution depends on the polarization plane of the incident light and vanishes for unpolarized light. From comparison of Eqs. (42) and (44) one can see that depending on the value of $\hbar\omega - E_g^{\text{QW}}$ the two contributions to $q_{xz'}$ can be comparable or one of them can dominate over the other.

The injection and control of pure spin currents in (110)-oriented GaAs QWs at room temperature by one-photon absorption of a linearly polarized optical pulse was demonstrated by Zhao et al. [86]. Spatially resolved

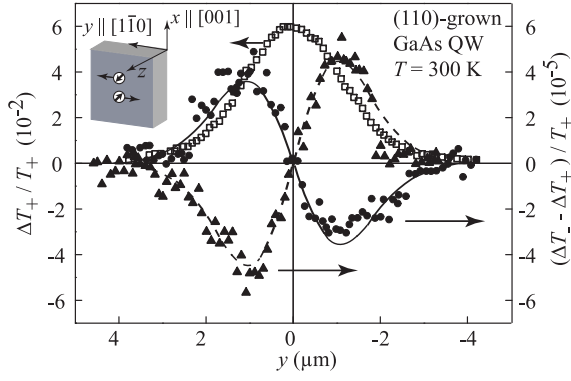


FIG. 13: Measurement of $\Delta T_+/T_+ \propto n_{-1/2}(y)$ (open squares) and $\Delta T_-/T_+ - \Delta T_+/T_+ \propto n_{1/2}(y) - n_{-1/2}(y)$ for an x polarized (solid circles) and a y polarized (solid triangles) pump pulse at room temperature for a pump fluence of $10 \mu\text{J}/\text{cm}^2$. The lines are the fits to the data for spin separation $d = 2.8 \text{ nm}$. After [86].

pump-probe technique was used. The pump pulse excited electrons from the valence to the conduction band with an excess energy of $\sim 148 \text{ meV}$ large enough for the polarization-dependent contribution (44) to dominate over the polarization independent contribution (42). The probe was tuned near the band edge. The σ_+ component of the linearly polarized probe interacts stronger with the spin-down electrons of the density $n_{-1/2}$, while the σ_- component interacts stronger with the spin-up electrons of the density $n_{1/2}$. Consequently, the net spin polarization of the carriers present in the sample at the position of the probe can be readily deduced from the difference in the transmission T_{\pm} of the σ_+ and σ_- components of the probe.

The results of measuring $n_{-1/2}(y) \propto \Delta T_+/T_+$ and $\Delta n(y) \equiv n_{1/2}(y) - n_{-1/2}(y) \propto \Delta T_-/T_+ - \Delta T_+/T_+$ for the x and y polarized pump are shown in Fig. 13. Note that here we retain the notations $x \parallel [001]$, $y \parallel [1\bar{1}0]$, $z \parallel [110]$ as they are introduced in the original paper [86] while in Eqs. (42) and (44) we use the Cartesian frame $x \parallel [1\bar{1}0]$, $y' \parallel [00\bar{1}]$, $z' \parallel [110]$. Clearly, the $\Delta n(y)$ signal is consistent with a pure spin current. It can be well fitted by the product of the spatial derivative of the original Gaussian profile and the separation d of the order of the photoelectron mean free path. The solid curve in Fig. 13 corresponds to a fit for $d = 28 \text{ \AA}$. In agreement with Eq. (44) the $\Delta n(y)$ signal has opposite signs for the x and y linear polarization of the pump.

It is worth to add that a pure spin current may be generated at simultaneous one- and two-photon coherent excitation of proper polarization as demonstrated in bulk GaAs [94] and GaAs/AlGaAs QWs [95]. This phenomenon may be attributed to a photogalvanic effect where the reduced symmetry is caused by the coherent two-frequency excitation [96].

B. Pure Spin Currents Due to Spin-Dependent Scattering

Light absorption by free carriers, or the Drude-like absorption, is accompanied by electron scattering by acoustic or optical phonons, static defects etc. Scattering-assisted photoexcitation with unpolarized light also gives rise to a pure spin current [88, 89]. However, in contrast to the direct transitions considered above, the spin splitting of the energy spectrum leads to no essential contribution to the spin current induced by free-carrier absorption. The more important contribution comes from asymmetry of the electron spin-conserving scattering. In gyrotropic low-dimensional structures, spin-orbit interaction adds an asymmetric spin-dependent term to the scattering probability. This term in the scattering matrix element is proportional to components of $[\boldsymbol{\sigma} \times (\mathbf{k} + \mathbf{k}')]_x$, where $\boldsymbol{\sigma}$ is the vector composed of the Pauli matrices, \mathbf{k} and \mathbf{k}' are the initial and scattered electron wave vectors.

Figure 14(b) sketches the process of energy relaxation of hot electrons for the spin-up subband ($s = +1/2$) in a quantum well containing a 2D electron gas. Energy relaxation processes are shown by curved arrows. Due to the spin-dependent scattering, transitions to positive and negative k'_x states occur with different probabilities. In Fig. 14(b) the difference is indicated by curved arrows of different thickness. This asymmetry causes an imbalance in the distribution of carriers in both subbands ($s = \pm 1/2$) between positive and negative k_x -states. This in turn yields a net electron flows, $\mathbf{i}_{\pm 1/2}$, within each spin subband. Since the asymmetric part of the scattering amplitude depends on spin orientation, the probabilities for scattering to positive or negative k'_x -states are inverted for spin-down and spin-up subbands. Thus, the charge currents, $\mathbf{j}_+ = e\mathbf{i}_{+1/2}$ and $\mathbf{j}_- = e\mathbf{i}_{-1/2}$, where e is the electron charge, have opposite directions because $\mathbf{i}_{+1/2} = -\mathbf{i}_{-1/2}$ and therefore they cancel each other. Nevertheless, a finite pure spin current $\mathbf{j}_s = (\mathbf{i}_{+1/2} - \mathbf{i}_{-1/2})/2$ is generated since electrons with spin-up and spin-down move in opposite directions [88].

Similarly to the relaxation mechanism, optical excitation of free carriers by Drude absorption, also involving electron scattering, is asymmetric and yields spin separation. Figure 14(a) sketches the process of Drude absorption via virtual states for the spin-up subband. Vertical arrow indicates optical transitions from the initial state with $k_x = 0$ while the horizontal arrows describe an elastic scattering event to a final state with either positive or negative electron wave vector. Due to the spin dependence of scattering, transitions to positive and negative k_x states occur with different probabilities. This is indicated by the different thickness of the horizontal arrows. The asymmetry causes an imbalance in the distribution of photoexcited carriers in the spin subband between positive and negative k_x -states. This in turn yields electron flow.

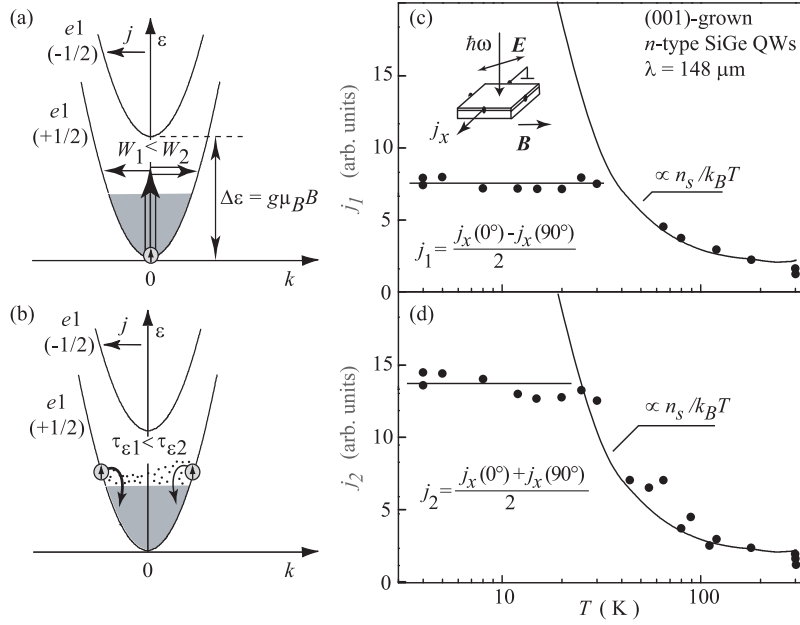


FIG. 14: Microscopic origin of a zero-bias spin separation and the corresponding magnetic field-induced photocurrent for excitation (a) and relaxation (b) models corresponding to currents j_1 and j_2 , see explanation in the text. Temperature dependencies of the contributions j_1 (c) and j_2 (d) to the photocurrent j_x in a magnetic field $\mathbf{B} \parallel y$. Full lines are fits to $An_s/k_B T$ with a single fitting parameter A , and to a constant, respectively. After [89].

1. Magneto-Gyrotropic Effects

A pure spin current and zero-bias spin separation can be converted into a measurable electric current by application of a magnetic field. Indeed, in a Zeeman spin-polarized system, the two fluxes $\mathbf{i}_{\pm 1/2}$, whose magnitudes depend on the free carrier densities in spin-up and spin-down subbands, $n_{\pm 1/2}$, respectively, do no longer compensate each other and hence yield a net electric current. Since the fluxes $\mathbf{i}_{\pm 1/2}$ are proportional to the carrier densities $n_{\pm 1/2}$ the charge current is given by

$$\mathbf{j} = e(\mathbf{i}_{1/2} + \mathbf{i}_{-1/2}) = 4eS\mathbf{j}_s, \quad (45)$$

where $x \parallel [1\bar{1}0], y \parallel [110]$, $S = (1/2)(n_{1/2} - n_{-1/2})/(n_{1/2} + n_{-1/2})$ is the average spin per particle and \mathbf{j}_s is the pure spin current in the absence of magnetic field. An external magnetic field \mathbf{B} results in different equilibrium populations of the two spin subbands due to the Zeeman effect. We remind that in equilibrium the average spin is given by $\mathbf{S} = -g\mu_B\mathbf{B}/4k_B T$ for a non-degenerate 2D electron gas and $\mathbf{S} = -g\mu_B\mathbf{B}/4E_F$ for a degenerate one, where μ_B is the Bohr magneton and g is the electron g -factor (or Landé factor).

In the structures of the C_{2v} symmetry, the phenomenological equation (5) for the magneto-photogalvanic effects induced by normally-incident linearly polarized radiation reduces to [97]

$$\begin{aligned} j_x &= S_1 B_y I + S_2 B_y (e_x^2 - e_y^2) I + 2S_3 B_x e_x e_y I, \\ j_y &= S'_1 B_x I + S'_2 B_x (e_x^2 - e_y^2) I + 2S'_3 B_y e_x e_y I. \end{aligned} \quad (46)$$

Here the parameters S_1 to S_3 and S'_1 to S'_3 are linearly independent components of the tensor $\Phi_{\lambda\mu\nu\eta}$ in Eq. (5) and only in-plane components of the magnetic field are taken into account. For $\mathbf{B} \parallel y$ we have

$$j_x = j_1 \cos 2\alpha + j_2, \quad j_y = j_3 \sin 2\alpha, \quad (47)$$

where $j_1 = S_2 B_y I$, $j_2 = S_1 B_y I$, $j_3 = S'_3 B_y I$.

Right panels of Fig. 14 show the temperature dependence of the currents j_1 and j_2 corresponding to the excitation and relaxation mechanisms depicted in Figs. 14(c) and 14(d), respectively. The data are obtained in an n -type SiGe QW structure for the magnetic field 0.6 T under excitation with a THz molecular laser ($\lambda = 148 \mu\text{m}$). The analysis shows [88, 89] that the temperature dependence of the current can be reduced to $n_s S$, the current becomes independent of temperature at low temperatures and is proportional to n_s/T at high temperatures, in agreement with the experimental data. Thus, the application of an external magnetic field gives experimental access to investigations of pure spin currents. The conversion of the pure spin current has been demonstrated for GaAs, InAs, InSb and Cd(Mn)Te QWs, for review see [98], as well as for Dirac fermions in HgTe QWs of critical thickness [99]. Like circular PGE and spin-galvanic effect, magneto-gyrotropic effect provides an efficient tool for investigation of inversion asymmetry as it is demonstrated for (110)-grown GaAs quantum wells [100].

C. Spin vs. Orbital Mechanisms of Photocurrents

While analyzing measured data on the polarization-dependent magneto-photogalvanic effects an attention should be paid to possible orbital mechanisms of the photocurrent formation [101–107]. Spin and orbital mechanisms may simultaneously be responsible for various physical phenomena and result in two competitive contributions to the observables. The textbook example is the Pauli paramagnetism and the Landau diamagnetism that yield comparable contributions to the magnetic susceptibility of an electron gas.

In addition to the spin mechanisms reviewed in this article, the photocurrents induced by circularly or linearly polarized radiation may also stem from orbital effects caused by quantum interference of optical transitions [108], ratchet effects in QWs with a lateral superlattice [109], dynamic Hall effect [110], pure valley currents [111], magnetic field dependent scattering [112] etc. It is worth recalling that, in the first papers [4, 5] on the circular PGE, Belinicher proposed an orbital mechanism of the effect whereas Ivchenko and Pikus predicted the spin-dependent circular photocurrent related to linear \mathbf{k} -terms in the free-carrier effective Hamiltonian. In materials with vanishingly small spin-orbit interaction, like Si or graphene, these mechanisms are obviously predominant.

An interplay of spin and orbital mechanisms has been demonstrated in GaAs/Al_xGa_{1-x}As QW structures [113] where the former contribution is proportional to the nonequilibrium spin while the latter is caused by a magnetic-field-induced and spin-independent scattering asymmetry. To separate them, the well-known fact that in GaAs based QWs the Zeeman splitting changes its sign at a certain QW width [2] has been utilized. This inversion is mostly caused by the opposite signs of the g -factor in bulk GaAs and AlGaAs and the deeper penetration of the electron wave function into the barrier with narrowing the QW width.

The experiment shows that for the most QW widths the magneto-gyrotropic PGE is mainly driven by spin-related mechanisms which result in a photocurrent proportional to the g -factor. For structures with a vanishingly small g -factor, i.e. for QW thicknesses close to the g -factor inversion point, the PGE caused by orbital mechanisms is clearly observed.

Experiments on (Cd,Mn)Te/(Cd,Mg)Te diluted magnetic semiconductor QWs [114] provide even more spectacular evidence for the zero-bias spin separation as a cause of the magneto-gyrotropic PGE. Diluted magnetic semiconductors (DMS) are traditionally defined as diamagnetic semiconductors doped with a few to several atomic percent of some transition metal with unpaired d electrons. Exchange interaction between the localized electrons of d shells of the magnetic ions and delocalized band carrier states gives rise to specific features of DMS, e.g., the exchange enhanced Zeeman splitting of the electronic bands and the giant Faraday rotation. Naturally,

the conversion of the zero-bias spin separation into the net electric current is also strongly affected by the magnetic properties of DMS structures.

The spin polarization of magnetic ions in an external magnetic field \mathbf{B} not only enhances the spin photocurrent due to the exchange enhanced Zeeman effect but also disturbs the balance between electron flows with opposite spins due to spin-dependent scattering by localized magnetic ions. The Zeeman splitting is given by a sum of intrinsic and exchange contributions of opposite signs, the former being independent of temperature and the latter being proportional to the modified Brillouin function $B_{5/2}(\xi)$, where

$$\xi = \frac{5}{2} \frac{g_{\text{Mn}} \mu_B B}{k_B (T_{\text{Mn}} + T_0)},$$

$g_{\text{Mn}} = 2$, T_{Mn} is the Mn-spin subsystem temperature and T_0 accounts for the Mn-Mn antiferromagnetic interaction. The strong temperature dependence of the exchange contribution governs the temperature behaviour of the spin photocurrent. In particular, it results in a reversal of the photocurrent direction with temperature variation. Experiments on Mn-doped II-VI, III-V, and hybrid III-V/II-VI QW structures excited by microwave or terahertz radiation have demonstrated that, as well as in other spin-dependent phenomena in DMS, the strength of photocurrent can be widely tuned by temperature, magnetic field and concentration of the magnetic ions.

VI. PHOTOCURRENTS OF DIRAC FERMIONS IN TOPOLOGICAL INSULATORS

In recent years, much attention in condensed-matter physics is directed towards studies of electronic properties of Dirac fermions in three-dimensional (3D) and 2D topological insulators (TI) which are nonmagnetic insulators in the “bulk” but have robust gapless edge/surface states described by a Dirac equation for massless particles.

Many materials have been proposed already as TIs, including the 3D family Bi₂Se₃, Bi₂Te₃, Sb₂Te₃ and their alloys, an alloy of Bi and Sb, narrow-gap semiconductor HgTe/CdTe and AlSb/InAs/GaSb/AlSb quantum wells, strained HgTe films as well as topological crystalline insulators Pb_{1-x}Sn_xSe [115, 116]. They are a new playground for many interesting phenomena in the spin physics. In particular, it has been demonstrated that the surface Dirac electron states have helical spin structure and possess a strong relationship between the charge current and spin polarization. The spin-dependent photogalvanic effects, direct and inverse, could not be better suited for establishing this relation [117–129].

McIver et al. [119] have shown that the illumination of the topological insulator Bi₂Se₃ with circularly polarized light generates a photocurrent originating from topological helical Dirac fermions and that the reversal of the light helicity reverses the direction of the photocurrent.

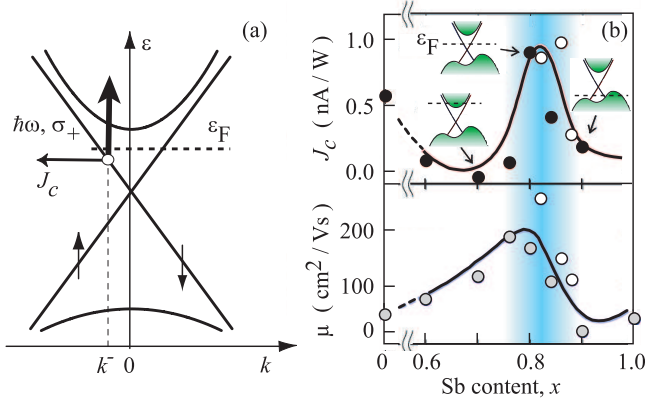


FIG. 15: (a) Schematic picture of optical transitions from helical edge states (straight lines marked by upward and downward arrows show spin-up and spin down branches, respectively) to bulk conduction band states (upper parabola). The vertical arrow illustrates asymmetry of the photoexcitation by circularly polarized radiation σ_+ : the probability of edge-bulk transition is spin-dependent and different for the spin-up and spin-down branches. Horizontal arrow sketches the resulting circular photocurrent, J_c . (b) The circular PGE current as a function of the Sb content x plotted together with the mobility. The $(\text{Bi}_{1-x}\text{Sb}_x)_2\text{Te}_3$ samples with the data represented with open circles were fabricated in a different chamber condition. The solid lines are guides to the eyes. The shaded area indicates the compositions where the Fermi energy ϵ_F is in the bulk band gap. The insets show the position of ϵ_F for three particular samples. After [126].

Later this effect has been observed for helical edge states of HgTe-based 2D TIs [129]. Furthermore, Olbrich et al. demonstrated that, by contrast to conventional QW structures discussed above, the spin-dependent photogalvanic effects in TI systems can even be generated by absorption of linearly polarized radiation [121].

An important advantage of the spin photogalvanics is that it, being forbidden by symmetry in most 3D TIs, can be used to probe selectively surface states of novel materials. This is particularly helpful in the search for room temperature 3D TI where transport experiments are often handicapped by a large residual bulk charge carrier density.

Photogalvanic currents originating from 2D surface states or one-dimensional helical edge states can be excited by different kinds of optical transitions including those between the edge and bulk states, the Drude absorption or the direct optical transitions between spin-up and spin-down branches of edge states characterized by linear dispersion. Figure 15(a) depicts the dispersion of helical dispersion of the edge states and the bulk conduction- and valence-band states (up and down parabolas). The edge/bulk mechanism of circular PGE [119, 123] schematically shown in Fig. 15(a) implements similar physical concepts as used for the photocurrents arising due to inter-subband optical transitions and discussed in Sect. II. Due to the spin-dependent selection

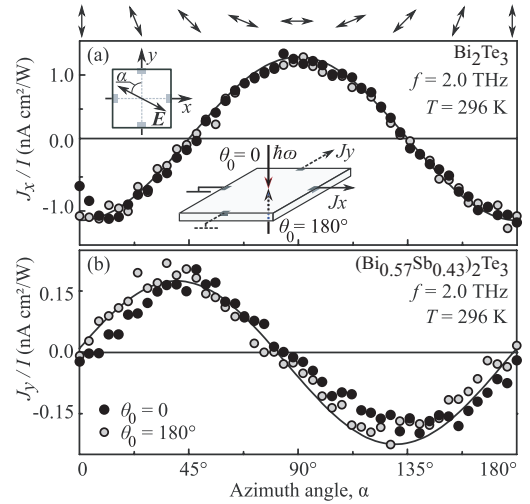


FIG. 16: (a) Photocurrent J_x/I measured in a Bi_2Te_3 sample. (b) Photocurrent J_y/I measured in a $(\text{Bi}_{0.57}\text{Sb}_{0.43})_2\text{Te}_3$ sample. Plots show the dependence of the photocurrent excited by normal incident radiation with $f = 2.0$ THz on the azimuth angle α . Angles of incidence $\theta_0 = 0$ and 180° correspond to the front and back excitations, respectively. Solid lines are best fits from the theory. Insets sketch the setup and the orientation of the electric field. Note that the photocurrent is probed in the directions coinciding with the principal axes of the trigonal system. After [127]

rules for the optical transitions, the photoionization from the spin-up and spin-down branches induced by circularly polarized radiation occurs with different rates. This is shown by the vertical arrow representing the “photoionization” of helical states, i.e. the depopulation of the Dirac cone and population of the excited bulk states. The resulting imbalance of the edge states population leads to a net electric current J_c .

Note that the photoexcited carriers can also contribute to the photocurrent but this contribution is small due to a fast relaxation of the bulk carriers. A series of $(\text{Bi}_{1-x}\text{Sb}_x)_2\text{Te}_3$ thin films were tailored so that the Fermi energy ϵ_F ranged from the bulk conduction-band bottom to the valence-band top through the surface-Dirac cone, see three insets in Fig. 15(b). The circular photogalvanic current, indicating a flow of spin-polarized surface-Dirac electrons, shows a pronounced peak when ϵ_F is set near the Dirac point, in correlation with the behaviour of carrier mobility.

The orientational and polarization analysis of the photocurrents in A_2B_3 TIs ($\text{A} = \text{Bi}, \text{Sb}$; $\text{B} = \text{Te}, \text{Se}$) and their alloys is based on their bulk point-group symmetry D_{3d} and the symmetry C_{3v} of the surface states, the latter, of course, for the trigonal axis C_3 being normal to the sample surface. At normal incidence, the C_{3v} point group forbids the circular PGE but allows the linear PGE. This is why the helicity-dependent photocurrent is observed only at oblique angle of incidence ($\theta_0 \neq 0, 180^\circ$) [119, 126], whereas the trigonal linear PGE is detected at any θ_0 [121, 127].

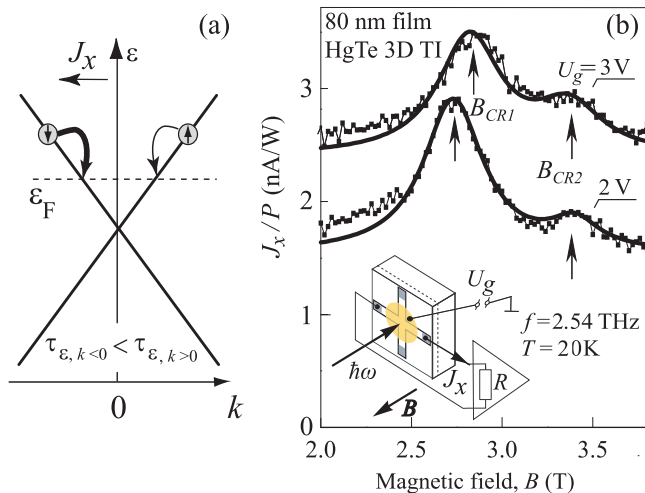


FIG. 17: (a) Microscopic origin of the cyclotron resonance induced spin photocurrent in 3D TI materials. (b) Magnetic field dependence of the photocurrent excited by circularly polarized THz radiation in a strained 80-nm HgTe 3D film. The numbers indicate applied gate voltages (Fermi level remains in the band gap). Inset shows the experimental geometry. The data for $V_g = 2$ V are multiplied by 4. After [128].

The D_{3d} group contains a center of space inversion and, thereby, forbids both the circular and linear photocurrents. However, a photon drag current can be generated in the centrosymmetric bulk as well. Under normal incidence of linearly polarized light, the azimuth-angle dependence of the photogenerated transverse current J_x or J_y is the same for the linear current of Dirac fermions and the drag current of bulk carriers. A straightforward way to distinguish the PGE response emerging from the surface states and the photon drag effect provides experiments with reversed direction of the light propagation: the former remains unchanged while the drag current has opposite directions in these two geometries. Inset in Fig. 16(a) indicates two normal geometries of incidence, $\theta_0 = 0$ and $\theta_0 = 180^\circ$. One can see that the photocurrents measured under the front and back illumination coincide which clearly demonstrates that, at normal incidence, the photon drag yields a minor contribution to the total photocurrent. At oblique incidence, however, in particular at large angles of incidence, the linear photocurrent can be outweighed by the photon drag effect in the surface states or in the bulk [127].

In 3D TIs based on strained HgTe films the strain opens a gap in the otherwise gapless HgTe which, together with the high quality of the material, allows one to obtain insulation in the bulk and study surface charge transport only [130, 131]. Figure 17 represents the observation of cyclotron resonance induced photocurrents generated in the surface states of a strained HgTe film sandwiched between thin $\text{Cd}_{0.65}\text{Hg}_{0.35}\text{Te}$ layers acting as capping and buffer layers [128]. Curved arrows in Fig. 17(a) indicate processes of carrier scattering. Their different thicknesses depict different scattering rates for the states

with oppositely oriented spins due to an asymmetric correction to these rates caused by the mixing of electron states by the magnetic field.

The asymmetry of carrier scattering in the momentum space leads to an electric current generation. Since the electron spin orientation in a topological surface state is locked to its momentum the observed photocurrents are spin polarized and accompanied by the emergence of a macroscopic surface spin polarization. The model of the photocurrent formation is supported by complementary measurements of the radiation transmission and magneto-transport, see for details Ref. [128].

The excitation of the sample with right-handed circularly polarized radiation (σ^+) and sweep of the magnetic field leads to two resonant dips at positive magnetic fields, Fig. 17(b). Upon changing the radiation helicity from σ^+ to σ^- the dips B_{CR1} and B_{CR2} appear at negative magnetic fields. For linearly polarized radiation, the resonances are observed for both magnetic field directions. These findings are clear signs that the absorption of radiation is caused by cyclotron resonance of electrons. From the dip position B_{CR} one can determine the corresponding cyclotron mass as follows

$$m_{CR} = \frac{|e|B_{CR}}{2\pi f c}, \quad (48)$$

where f is the light frequency. At $T = 40$ K the masses $m_{CR} = 0.028m_0$ and $0.035m_0$ are obtained for dips at $B_{CR} = 2.6$ and 3.35 T, respectively. The two values of m_{CR} correspond to the top and bottom interfaces, they are different because of a built-in electric field. It is very important to stress that the cyclotron resonance of the bulk carriers is expected at substantially higher magnetic fields corresponding to a mass of about $0.07m_0$.

VII. CIRCULAR PHOTO GALVANIC EFFECT IN WEYL SEMIMETALS

In the theoretical works [132–135] the CPGE is studied in the Weyl semimetals. It is established that the contribution of each Weyl node to the circular photocurrent takes the universal form [132]

$$\mathbf{j} = C\Gamma_0\tau_p\mathbf{i}(\mathbf{E} \times \mathbf{E}^*), \quad (49)$$

where $\Gamma_0 = \pi e^3/3h^2$, e is the electron charge, h is the Planck constant, $C = \pm 1$ is the chirality (or topological charge) of the node, τ_p is the electron momentum relaxation time. The universality of Eq. (49) means that, with the exception of the factor τ_p , the right-hand side of this equation contains a numerical factor $\pi/3$ and the world constants e and h . Ching-Kit Chan et al. [133] have considered a pair of Weyl nodes with opposite chiralities. They have shown that the contributions to the circular photocurrent do not cancel each other provided that, in addition to the terms $A_{\alpha\beta}\sigma_\alpha k_\beta$, the effective electron Hamiltonian contains the tilt term $\mathbf{a} \cdot \mathbf{k}$ with the vector

\mathbf{a} different in the different nodes where \mathbf{k} is the electron wave vector referred to the node \mathbf{k}_W . However, in this case the equation for the photocurrent loses its universality. Recently Qiong Ma et al. [136] have observed a circular photocurrent in the TaAs crystal under excitation by CO₂ laser radiation.

Golub et al. [135] have analyzed how the presence of a reflection plane in the point-symmetry group of a gyrotropic crystal affects the CPGE and discussed the influence of a magnetic field on the photocurrents in Weyl gyrotropic semimetals. A particular attention is paid to the crystal classes C_{4v} and C_{2v}. The effective electron Hamiltonian near the Weyl node \mathbf{k}_W is given in the form

$$\mathcal{H} = \mathbf{d}(\mathbf{k}) \cdot \boldsymbol{\sigma} + d_0(\mathbf{k})\sigma_0, \quad (50)$$

where σ_0 is the identity matrix of dimension 2, $d_l(\mathbf{k})$ ($l = 0, x, y, z$) are functions whose expansions in powers of \mathbf{k} contain no terms of the zero order. The eigenenergies of this Hamiltonian take on the values $E_{\pm, \mathbf{k}} = d_0(\mathbf{k}) \pm d(\mathbf{k})$, where $d(\mathbf{k}) = |\mathbf{d}(\mathbf{k})|$. Hereafter the energy is referred to the electron energy at the Weyl point. Usually, for simplicity only linear terms are taken into account in $d_0(\mathbf{k})$: $d_0(\mathbf{k}) = \mathbf{a} \cdot \mathbf{k}$, where \mathbf{a} is some vector. This term describes the tilt of the Weyl cone.

Under direct optical transitions in the vicinity of the \mathbf{k}_W point, the following photocurrent is generated

$$\mathbf{j} = e \sum_{\mathbf{k}} \tau_p \frac{2}{\hbar} \frac{\partial d(\mathbf{k})}{\partial \mathbf{k}} W_{+-}(\mathbf{k}), \quad (51)$$

where the rate of optical transitions per unit volume per unit time is given by

$$W_{+-} = \frac{2\pi}{\hbar} |M_{+-}|^2 F(\mathbf{k}) \delta(2d - \hbar\omega), \quad (52)$$

M_{+-} is the matrix element of the optical transition that does not depend on $d_0(\mathbf{k})$,

$$F(\mathbf{k}) = f(E_{-, \mathbf{k}}) - f(E_{+, \mathbf{k}}), \quad (53)$$

$f(E)$ is the equilibrium Fermi-Dirac distribution function. The factor 2 in Eq. (51) takes into account the contributions to the current from the photoelectrons and photoholes. Similarly to Ref. [132], one can show that, under the circularly polarized excitation, the polarization-dependent contribution to the square modulus of the matrix element is proportional to the Berry curvature

$$|M_{+-}|_{\text{circ}}^2 = \frac{2e^2 d^2}{(\hbar\omega)^2} |\mathbf{E}|^2 \boldsymbol{\kappa} \cdot \boldsymbol{\Omega}, \quad (54)$$

where $\boldsymbol{\kappa} = i(\mathbf{e} \times \mathbf{e}^*)$, \mathbf{e} is a unit polarization vector, the Berry curvature is related to the vector $\mathbf{d}(\mathbf{k})$ by

$$\boldsymbol{\Omega}_j = \frac{\mathbf{d}}{2d^3} \cdot \left(\frac{\partial \mathbf{d}}{\partial k_{j+1}} \times \frac{\partial \mathbf{d}}{\partial k_{j+2}} \right), \quad (55)$$

and the cyclic permutation of the indices is assumed. We note that, taking into account the energy conservation

law, the argument $E_{\pm, \mathbf{k}}$ of the distribution function can be replaced by $d_0(\mathbf{k}) \pm \hbar\omega/2$. Therefore, for a fixed frequency ω , the difference of occupation numbers (53) is a function of the scalar $d_0(\mathbf{k})$.

The structure of the second-rank pseudotensor γ in Eq. (1) for all 18 gyrotropic classes is well known, see e.g. [137]. The question arises what is the simplest form of the Hamiltonian (50) which satisfies the two requirements: (i) it leads to a nonzero contribution of the node \mathbf{k}_W to the $\gamma_{\alpha\beta}$ tensor which is allowed by the crystal symmetry group F , and (ii) this contribution does not disappear after the summation over the star of the vector \mathbf{k}_W .

First we consider *gyrotropic classes that do not contain reflection planes*, and take into account in the Hamiltonian (50) only terms linear in \mathbf{k} : $d_\alpha = A_{\alpha\beta} k_\beta$, with the chirality of the node \mathbf{k}_W equal to $\text{sgn}\{\text{Det}(\hat{\mathbf{A}})\}$. In this case all the Weyl nodes obtained by the symmetry transformations are characterized by the same chirality. In the absence of a tilt, $d_0(\mathbf{k}) = 0$, the tensor γ is isotropic: the off-diagonal components are absent, while the diagonal components coincide and are equal to the contribution of a single node (49) multiplied by the number of vectors n in the star of the vector \mathbf{k}_W if this star contains the vector $-\mathbf{k}_W$, and $2n$ if \mathbf{k}_W and $-\mathbf{k}_W$ belong to different stars. The doubling is due to the symmetry to the time inversion which transforms the point \mathbf{k}_W to $-\mathbf{k}_W$ preserving the chirality. The difference in the diagonal components allowed by the symmetry is obtained taking account of the tilt.

To calculate the off-diagonal components $\gamma_{\alpha\beta}$ in crystals of the symmetries C₁ and C₂, one needs to take into account the tilt with nonzero coefficients a_α and a_β . In the Hamiltonian with linear- \mathbf{k} terms, the off-diagonal components $\gamma_{xy} = -\gamma_{yx}$ in the classes C₃, C₄ and C₆ are not obtained, even with allowance for the tilt.

The gyrotropic classes containing reflection planes, only linear- \mathbf{k} terms in the Hamiltonian are taken into account. The off-diagonal components of $\gamma_{\alpha\beta}$ in the groups C_s, C_{2v}, S₄ and the diagonal components $\gamma_{xx} = -\gamma_{yy}$ in the groups S₄, D_{2d} arise in the calculation with allowance for the tilt. In the groups C_{3v}, C_{4v} and C_{6v}, nonzero off-diagonal components do not appear in the linear Hamiltonian model with an arbitrary tilt function $d_0(\mathbf{k})$.

Thus, the six gyrotropic classes C_n, C_{nv} ($n = 3, 4, 6$) stand apart from the rest: for them the components $\gamma_{xy} = -\gamma_{yx}$ can be obtained by adding, to the spin-dependent part of \mathcal{H} , terms of the higher (second or third) order in \mathbf{k} . In the $\mathbf{k} \cdot \mathbf{p}$ method, the nonlinear terms in $\mathbf{d}(\mathbf{k})$ arise from the contribution of remote bands in the perturbation theory and, therefore, can be considered as being small compared to the linear terms.

One more effect specific for gyrotropic media is a magneto-induced photocurrent independent of the light polarization. In this effect, in the linear in magnetic field approximation, the polar vector – the photocurrent density – is related with the axial vector – the magnetic field. For example, the following currents are generated

in crystals of the C_{2v} symmetry [135]

$$\begin{aligned} j_x &= (S_{xx}B_x + S_{xy}B_y) |\mathbf{E}|^2, \\ j_y &= -(S_{xx}B_y + S_{xy}B_x) |\mathbf{E}|^2, \end{aligned} \quad (56)$$

where the Cartesian coordinate system is chosen with the axis $z \parallel C_2$ and the axis x composing the angle 45° with the reflection planes σ_v .

VIII. CONCLUDING REMARKS

The two main fields of study in the modern physics of semiconductors are transport phenomena and optical effects. Sometimes an impression arises that, founded on much the same basis of tremendous successes achieved in technology, these fields are developing independently of each other. It is also true for the extensive studies of spin physics in semiconductors. One of the aims of this review is to show that the spin photogalvanics builds a solid bridge between the two fields and sets up a base for the reciprocation of ideas. Indeed, the spin-dependent photogalvanic effects, including charge and spin photocurrents, as well as the inverse effects allowing optical detection of current-induced spin polarization need a thorough knowledge in both the transport physics and the polarized optical spectroscopy. As a result the different concepts supplement each other and provide a deeper insight in the spin-dependent microscopic processes.

Since the observation of the circular photogalvanic effect in GaAs quantum wells at the turn of the millennium [8], a coupling of photo-induced nonequilibrium spin to the directed electron motion has been demonstrated for a great variety of semiconductor low-dimensional systems. Experiments and theoretical developments demonstrated that spin-dependent optical excitation or spin-dependent relaxation of nonequilibrium carriers may cause an electric current as well as result in a pure spin current. The family of spin photogalvanics includes a number of phenomena such as the circular photogalvanic effect, spin-galvanic effect and its inversion, zero-bias spin separation, magneto-gyrotropic effect etc. The form of second-rank tensors $\boldsymbol{\gamma}$, \mathbf{Q} , \mathbf{R} and the fourth-rank tensor $\boldsymbol{\Phi}$ describing these effects, i.e. the

number of their nonzero components and possible relations between them, is fully determined by the space and time-inversion symmetry of the system. Therefore, the photocurrent measurements are a convenient tool for the determination or confirmation of the point-group symmetries of bulk crystals or nanoheterostructures.

At present the spin photogalvanics has become a scientific measurement platform for the manifestations of various spin-dependent effects, such as the optical orientation of electronic spins, the Hanle effect, the exchange enhanced Zeeman effect in diluted magnetic semiconductors, the cyclotron resonance of topologically protected surface states, coherent Zitterbewegung etc. As a result, the various band-structure and kinetic parameters can be readily and independently extracted from the photocurrent measurements.

As for the future work, the most challenging tasks are (i) the investigation of spin photogalvanics beyond perturbation limit at extremely high power optical excitation and (ii) the analysis of the photocurrent dynamics in time resolved experiments. Nonperturbative photogalvanics is expected to be characterized by a nontrivial behavior of the photocurrent on the light intensity and polarization state. This study should lead to the observation of the photovoltaic Hall effect at zero magnetic field and edge photocurrents caused by the nontrivial topology of Floquet states as well as would allow one to explore the energy spectrum reconstruction by intense THz electric fields due to formation of Floquet topological insulators and dressed states.

Time resolved experiments on spin photogalvanics under photoexcitation with femtosecond pulses, i.e. with the pulse duration being comparable with the free-carrier momentum relaxation time, would be desirable and informative for deep analysis of the individual photocurrent mechanisms like shift vs. ballistic or spin vs. orbital effects. Such study would also reveal a great deal about the momentum, energy and spin relaxation of nonequilibrium photoexcited carriers. A technical realization of these challenging experiments becomes possible most recently and is, similarly to the Auston-switch, based on study of terahertz radiation emitted by current pulses by means of THz time domain spectroscopy.

-
- [1] F. Meier, B.P. Zakharchenya (eds.), *Optical Orientation* (North-Holland, Amsterdam, 1984)
 - [2] E.L. Ivchenko, *Optical Spectroscopy of Semiconductor Nanostructures* (Alpha Science, Harrow, 2005)
 - [3] S.D. Ganichev, M. Trushin, J. Schliemann, Spin Polarisation by Current, in *Handbook of Spin Transport and Magnetism*, eds. E.Y. Tsybal, I. Zutic (Chapman and Hall, 2011); arXiv:1606.02043 [cond-mat.mes-hall]
 - [4] E.L. Ivchenko and G.E. Pikus, Pis'ma Zh. Eksp. Teor. Fiz. **27**, 640 (1978); JETP Lett. **27**, 604 (1978)
 - [5] V.I. Belinicher, Phys. Lett. A **66**, 213 (1978)
 - [6] V.M. Asnin, A.A. Bakun, A.M. Danishevskii, E.L. Ivchenko, G.E. Pikus, A.A. Rogachev, Pis'ma Zh. Eksp. Teor. Fiz. **28**, 80 (1978); JETP Lett. **28**, 74 (1978)
 - [7] B.I. Sturman, V.M. Fridkin, *The Photovoltaic and Photo-refractive Effects in Non-Centrosymmetric Materials* (Gordon and Breach Science Publishers, Philadelphia, 1992)
 - [8] S.D. Ganichev, H. Ketterl, W. Prettl, E.L. Ivchenko, L.E. Vorobjev, Appl. Phys. Lett. **77**, 3146 (2000)
 - [9] S.D. Ganichev, E.L. Ivchenko, S.N. Danilov, J. Eroms,

- W. Wegscheider, D. Weiss, W. Prettl, Phys. Rev. Lett. **86**, 4358 (2001)
- [10] S.D. Ganichev, W. Prettl, J. Phys.: Condens. Matter **15**, 935 (2003)
- [11] S.D. Ganichev, W. Prettl, *Intense Terahertz Excitation of Semiconductors* (Oxford University Press, Oxford, 2006)
- [12] S.D. Ganichev, V.V. Bel'kov, Petra Schneider, E.L. Ivchenko, S.A. Tarasenko, D. Schuh, W. Wegscheider, D. Weiss, W. Prettl, Phys. Rev. B **68**, 035319 (2003)
- [13] V. A. Shalygin, H. Diehl, Ch. Hoffmann, S.N. Danilov, T. Herrle, S.A. Tarasenko, D. Schuh, Ch. Gerl, W. Wegscheider, W. Prettl, S.D. Ganichev, Pis'ma Zh. Eksp. Teor. Fiz. **84**, 666 (2006); JETP Lett. **84**, 570 (2006)
- [14] B. Wittmann, S.N. Danilov, V.V. Bel'kov, S.A. Tarasenko, E.G. Novik, H. Buhmann, C. Brüne, L.W. Molenkamp, Z.D. Kvon, N.N. Mikhailov, S.A. Dvoret'sky, N.Q. Vinh, A.F.G. van der Meer, B. Murdin, S.D. Ganichev, Semicond. Sci. Technol. **25**, 095005 (2010)
- [15] M.I. Dyakonov, V.Yu. Kachorovskii, Fiz. Tekh. Poluprovodn. **20**, 178 (1986); Sov. Phys. Semicond. **20**, 110 (1986)
- [16] G. Dresselhaus, Phys. Rev. **100**, 580 (1955).
- [17] F.T. Vasko, Pis'ma Zh. Eksp. Teor. Fiz., 30, 574 (1979); JETP Lett., 30, 541 (1979)
- [18] Y.A. Bychkov, E.I. Rashba, Pis'ma Zh. Eksp. Teor. Fiz. **39**, 66 (1984); JETP Lett. **39**, 78 (1984)
- [19] R. Winkler, *Spin-Orbit Coupling Effects in Two-Dimensional Electron and Hole Systems*, Springer Tracts in Modern Physics, vol. 191 (Springer, Berlin, 2003)
- [20] W. Zawadzki, P. Pfeffer, Semicond. Sci. Technol. **19**, R1 (2004)
- [21] O. Krebs, P. Voisin, Phys. Rev. Lett. **77**, 1829 (1996)
- [22] U. Rössler, J. Keinz, Solid State Commun. **121**, 313 (2002)
- [23] M.O. Nestoklon, E.L. Ivchenko, P. Voisin, Phys. Rev. B **77**, 155328 (2008)
- [24] S.D. Ganichev, L.E. Golub, Phys. Stat. Sol. B **251**, 1801 (2014)
- [25] V.V. Bel'kov, S.D. Ganichev, Petra Schneider, C. Back, M. Oestreich, J. Rudolph, D. Hägele, L.E. Golub, W. Wegscheider, W. Prettl, Solid State Commun. **128**, 283 (2003)
- [26] M. Bieler, N. Laman, H.M. van Driel, A.L. Smirl, Appl. Phys. Lett. **86**, 061102 (2005)
- [27] C.L. Yang, H.T. He, Lu Ding, L.J. Cui, Y.P. Zeng, J.N. Wang, W.K. Ge, Phys. Rev. Lett. **96**, 186605 (2006)
- [28] K.S. Cho, Y.F. Chen, Y.Q. Tang, B. Shen, Appl. Phys. Lett. **90**, 041909 (2007)
- [29] J.L. Yu, Y.H. Chen, C.Y. Jiang, Y. Liu, H. Ma, J. Appl. Phys. **109**, 053519 (2011)
- [30] J. L. Yu, Y. H. Chen, Y. Liu, C.Y. Jiang, H. Ma, L. P. Zhu, Appl. Phys. Lett. **100**, 152110 (2012)
- [31] Jinling Yu, Shuying Cheng, Yunfeng Lai, Qiao Zheng, Laipan Zhu, Yonghai Chen, Jun Ren, Opt. Express **23**, 027250 (2015)
- [32] Z. Zhang, R. Zhang, B. Liu, Z.L. Xie, X.Q. Xiu, P. Han, H. Lu, Y.D. Zheng, Y.H. Chen, C.G. Tang, Z.G. Wang, Solid State Commun. **145** 159 (2008)
- [33] N. Ogawa, M.S. Bahramy, Y. Kaneko, Y. Tokura, Phys. Rev. B **90**, 125122 (2014)
- [34] L.E. Golub, Phys. Rev. B **67**, 235320 (2003)
- [35] E. Deyo, L.E. Golub, E.L. Ivchenko, B. Spivak, arXiv:0904.1917
- [36] J.E. Moore, J. Orenstein, Phys. Rev. Lett. **105**, 026805 (2010)
- [37] S.D. Ganichev, S.N. Danilov, V.V. Bel'kov, E.L. Ivchenko, M. Bichler, W. Wegscheider, D. Weiss, W. Prettl, Phys. Rev. Lett. **88**, 057401 (2002)
- [38] P. Schneider, J. Kainz, S.D. Ganichev, V.V. Bel'kov, S.N. Danilov, M.M. Glazov, L.E. Golub, U. Rössler, W. Wegscheider, D. Weiss, D. Schuh, W. Prettl, J. Appl. Phys. **96**, 420 (2004)
- [39] M.I. Dyakonov, V.I. Perel, Zh. Eksp. Teor. Fiz. **60**, 1954 (1971); Sov. Phys. JETP **33**, 1053 (1971)
- [40] E.L. Ivchenko, Yu.B. Lyanda-Geller, G.E. Pikus, Pis'ma Zh. Eksp. Teor. Fiz. **50**, 156 (1989); JETP Lett. **50**, 175 (1989)
- [41] S.D. Ganichev, E.L. Ivchenko, V.V. Bel'kov, S.A. Tarasenko, M. Sollinger, D. Weiss, W. Wegscheider, W. Prettl, Nature (Lond.) **417**, 153 (2002)
- [42] N.S. Averkiev, L.E. Golub, M. Willander, J. Phys.: Condens. Matter **14**, R271 (2002)
- [43] S.D. Ganichev, Petra Schneider, V.V. Bel'kov, E.L. Ivchenko, S.A. Tarasenko, W. Wegscheider, D. Weiss, D. Schuh, D.G. Clarke, M. Merrick, B.N. Murdin, P. Murzyn, P.J. Phillips, C.R. Pidgeon, E.V. Beregul'in, W. Prettl, Phys. Rev. B **68**, 081302 (2003)
- [44] R. J. Elliott, Phys. Rev. **96**, 266 (1954).
- [45] Y. Yafet, in Solid State Physics, vol. 14, ed. by F. Seitz, D. Turnbull (Academic, New York, 1963), p. 1.
- [46] L.E. Golub, Pis'ma Zh. Eksp. Teor. Fiz. **85**, 479 (2007); JETP Lett. **85**, 393 (2007)
- [47] A.A. Burkov, A.S. Núñez, A. H. MacDonald, Phys. Rev. B **70**, 155308 (2004)
- [48] S.A. Tarasenko, E.L. Ivchenko, V.V. Bel'kov, S.D. Ganichev, D. Schowalter, Petra Schneider, M. Sollinger, W. Prettl, V.M. Ustinov, A.E. Zhukov, L.E. Vorobjev, J. Supercond.: Incorporating Novel Magn. **16**, 419 (2003)
- [49] A.A. Bakun, B.P. Zakharchenya, A.A. Rogachev, M.N. Tkachuk, V.G. Fleisher, Pis'ma ZhETF **40**, 464 (1984); Sov. JETP Lett. **40**, 1293 (1984)
- [50] N.S. Averkiev, M.I. Dyakonov, Fiz. Tekh. Poluprov. **17**, 629 (1983); Sov. Phys. Semicond. **17**, 393 (1983)
- [51] M.I. Dyakonov, V.I. Perel', Pis'ma ZhETF **13**, 206 (1971); Sov. JETP Lett. **13**, 144 (1971)
- [52] E.L. Ivchenko, S.A. Tarasenko, Zh. Eksp. Teor. Fiz. **126**, 426 (2004); JETP **99**, 379 (2004)
- [53] S.D. Ganichev, V.V. Bel'kov, L.E. Golub, E.L. Ivchenko, Petra Schneider, S. Giglberger, J. Eroms, J. De Boeck, G. Borghs, W. Wegscheider, D. Weiss, W. Prettl, Phys. Rev. Lett. **92**, 256601 (2004)
- [54] S. Giglberger, L.E. Golub, V.V. Bel'kov, S.N. Danilov, D. Schuh, Ch. Gerl, F. Rohlfing, J. Stahl, W. Wegscheider, D. Weiss, W. Prettl, S.D. Ganichev, Phys. Rev. B **75** 035327 (2007)
- [55] M. Kohda, V. Lechner, Y. Kunihashi, T. Dollinger, P. Olbrich, C. Schönhuber, I. Caspers, V.V. Bel'kov, L.E. Golub, D. Weiss, K. Richter, J. Nitta, S.D. Ganichev, Phys. Rev. B **86**, 081306 (2012)
- [56] I. Stepanov, M. Ersfeld, A.V. Poshakinskiy, M. Lepsa, E.L. Ivchenko, S.A. Tarasenko, B. Beschoten, submitted

- [57] L.E. Vorob'ev, E.L. Ivchenko, G.E. Pikus, I.I. Farbstain, V.A. Shalygin, A.V. Sturbin, Pis'ma Zh. Eksp. Teor. Fiz. **29**, 485 (1979); JETP Lett. **29**, 441 (1979)
- [58] V.A. Shalygin, A.N. Sofronov, L.E. Vorob'ev, I.I. Farbstain, Fiz. Tverd. Tela **54**, 2237 (2012); Phys. Solid State **54**, 2362 (2012)
- [59] F.T. Vasko and N.A. Prima, Fiz. Tverd. Tela **21**, 1734 (1979) [Sov. Phys. Solid State **21**, 994 (1979)].
- [60] L.S. Levitov, Yu.V. Nazarov, and G.M. Eliashberg, Zh. Eksp. Teor. Fiz. **88**, 229 (1985); Sov. Phys. JETP **61**, 133 (1985)
- [61] A.G. Aronov, Yu.B. Lyanda-Geller, Pis'ma Zh. Eksp. Teor. Fiz. **50**, 398 (1989); JETP Lett. **50**, 431 (1989)
- [62] V.M. Edelstein, Solid State Commun. **73**, 233 (1990)
- [63] A.G. Aronov, Yu.B. Lyanda-Geller, G.E. Pikus, Zh. Eksp. Teor. Fiz. **100**, 973 (1991); Sov. Phys. JETP **73**, 537 (1991)
- [64] A.V. Chaplik, M.V. Entin, L.I. Magarill Physica E **13**, 744 (2002)
- [65] F.T. Vasko, O.E. Raichev, *Quantum Kinetic Theory and Applications* (Springer, New York, 2005).
- [66] S.A. Tarasenko, Pis'ma Zh. Eksp. Teor. Fiz. **84**, 233 (2006); JETP Lett. **84**, 199 (2006)
- [67] M. Trushin, J. Schliemann, Phys. Rev. B **75**, 155323 (2007)
- [68] O.E. Raichev, Phys. Rev. B **75**, 205340 (2007)
- [69] S.A. Tarasenko, Physica E **40**, 1614 (2008)
- [70] L.E. Golub, E.L. Ivchenko, Phys. Rev. B **84**, 115303 (2011)
- [71] D. Guerzi, J. Borge, R. Raimondi, Physica E **82** 151 (2016)
- [72] C. Gorini, A. Maleki, Ka Shen, I.V. Tokatly, G. Vignale, and R. Raimondi, arXiv:1702.04887v1 (2017)
- [73] S.D. Ganichev, S.N. Danilov, Petra Schneider, V.V. Bel'kov, L.E. Golub, W. Wegscheider, D. Weiss, W. Prettl, arXiv:0403641 (2004), see also J. Magn. and Magn. Materials **300**, 127 (2006)
- [74] A.Yu. Silov, P.A. Blajnov, J.H. Wolter, R. Hey, K.H. Ploog, N.S. Averkiev, Appl. Phys. Lett. **85**, 5929 (2004)
- [75] Y.K. Kato, R.C. Myers, A.C. Gossard, D.D. Awschalom, Phys. Rev. Lett. **93**, 176601 (2004)
- [76] A.Yu. Silov, P.A. Blajnov, J.H. Wolter, R. Hey, K.H. Ploog, and N.S. Averkiev, in *Proc. 13th Int. Symp. Nanostructures: Phys. and Technol.*, (St. Petersburg, Russia, 2005)
- [77] V. Sih, R.C. Myers, Y.K. Kato, W.H. Lau, A.C. Gossard, D.D. Awschalom, Nat. Phys. **1**, 31 (2005)
- [78] N.P. Stern, S. Ghosh, G. Xiang, M. Zhu, N. Samarth, D.D. Awschalom, Phys. Rev. Lett. **97**, 126603 (2006)
- [79] S. Kuhlén, K. Schmalbuch, M. Hagedorn, P. Schlamme, M. Patt, M. Lepsa, G. Güntherodt, and B. Beschoten, Phys. Rev. Lett. **109**, 146603 (2012)
- [80] B.M. Norman, C.J. Trowbridge, D.D. Awschalom, V. Sih, Phys. Rev. Lett. **112**, 056601 (2014)
- [81] L.E. Golub, E.L. Ivchenko, New J. Phys. **15**, 125003 (2013)
- [82] D.S. Smirnov and L.E. Golub, Phys. Rev. Lett. **118**, 116801 (2017)
- [83] D.D. Awschalom, D. Loss, N. Samarth (eds.), *Semiconductor Spintronics and Quantum Computation* (Springer, Berlin, 2002)
- [84] R.D.R. Bhat, F. Nastos, A. Najmaie, J.E. Sipe, Phys. Rev. Lett. **94**, 096603 (2005)
- [85] S.A. Tarasenko, E.L. Ivchenko, Pis'ma Zh. Eksp. Teor. Fiz. **81**, 292 (2005); JETP Lett. **81**, 231 (2005)
- [86] H. Zhao, X. Pan, A.L. Smirl, R.D.R. Bhat, A. Najmaie, J.E. Sipe, H.M. van Driel, Phys. Rev. B **72** 201302 (2005)
- [87] Bin Zhou, Shun-Qing Shen, Phys. Rev. B **75**, 045339 (2007)
- [88] S.D. Ganichev, V.V. Bel'kov, S.A. Tarasenko, S.N. Danilov, S. Giglberger, Ch. Hoffmann, E.L. Ivchenko, D. Weiss, W. Wegscheider, Ch. Gerl, D. Schuh, J. Stahl, J.De Boeck, G. Borghs, W. Prettl, Nat. Phys. **2**, 609 (2006)
- [89] S.D. Ganichev, S.N. Danilov, V.V. Bel'kov, S. Giglberger, S.A. Tarasenko, E.L. Ivchenko, D. Weiss, W. Jantsch, F. Schäffler, D. Gruber, W. Prettl, Phys. Rev. B **75**, 155317 (2007)
- [90] S.A. Tarasenko, E.L. Ivchenko, Proc. ICPS-28 (Vienna, 2006), AIP Conf. Proc. **893**, 1331 (2007); cond-mat/0609090
- [91] E.L. Ivchenko, A.A. Toropov, P. Voisin, Fiz. Tverd. Tela **40**, 1925 (1989); Phys. Solid State **40**, 1748 (1998)
- [92] J.B. Khurgin, Phys. Rev. B **73**, 033317 (2006)
- [93] J.-M. Jancu, R. Scholz, E.A. de Andrada e Silva, G.C. La Rocca, Phys. Rev. B **72**, 193201 (2005)
- [94] M.J. Stevens, A.L. Smirl, R.D.R. Bhat, J.E. Sipe, H.M. van Driel, J. Appl. Phys. **91**, 4382 (2002)
- [95] M.J. Stevens, A.L. Smirl, R.D.R. Bhat, A. Najmaie, J.E. Sipe, H.M. van Driel, Phys. Rev. Lett. **90**, 136603 (2003)
- [96] M.V. Entin, Fiz. Tekh. Poluprov. **23**, 1066 (1989); Sov. Phys. Semicond. **23**, 664 (1989)
- [97] V.V. Bel'kov, S.D. Ganichev, E.L. Ivchenko, S.A. Tarasenko, W. Weber, S. Giglberger, M. Olteanu, P. Tranitz, S.N. Danilov, Petra Schneider, W. Wegscheider, D. Weiss, W. Prettl, J. Phys.: Condens. Matter **17**, 3405 (2005)
- [98] V.V. Bel'kov, S.D. Ganichev, *Zero-bias spin separation*, in *Handbook of Spintronic Semiconductors*, eds. W.M. Chen and I.A. Buyanova (Pan Stanford Publishing 2010)
- [99] P. Olbrich, C. Zoth, P. Vierling, K.-M. Dantscher, G.V. Budkin, S.A. Tarasenko, V.V. Bel'kov, D.A. Kozlov, Z.D. Kvon, N.N. Mikhailov, S.A. Dvoretzky, S.D. Ganichev, Phys. Rev. B **87**, 235439 (2013)
- [100] V.V. Bel'kov, P. Olbrich, S.A. Tarasenko, D. Schuh, W. Wegscheider, T. Korn, C. Schüller, D. Weiss, W. Prettl, S.D. Ganichev, Phys. Rev. Lett. **100**, 176806 (2008)
- [101] E.L. Ivchenko, B. Spivak, Phys. Rev. B **66**, 155404 (2002)
- [102] S.A. Tarasenko, Pis'ma Zh. Eksp. Teor. Fiz. **85**, 216 (2007); JETP Lett. **85**, 182 (2007)
- [103] J. Karch, S.A. Tarasenko, P. Olbrich, T. Schönberger, C. Reitmaier, D. Plohmann, Z.D. Kvon, S.D. Ganichev, J. Phys.: Condens. Matter **22**, 355307 (2010)
- [104] S.A. Tarasenko, Phys. Rev. B **83**, 035313 (2011)
- [105] C. Drexler, S.A. Tarasenko, P. Olbrich, J. Karch, M. Hirmer, F. Müller, M. Gmitra, J. Fabian, R. Yakimova, S. Lara-Avila, S. Kubatkin, M. Wang, R. Vajtai, P. M. Ajayan, J. Kono, and S.D. Ganichev, Nature Nanotechnol. **8**, 104 (2013)
- [106] S. Dhara, E.J. Mele, R. Agarwal, Science **349**, 726 (2015)

- [107] N. Kheirabadi, E. McCann, V.I. Fal'ko, arXiv:1606.08234
- [108] P. Olbrich, S.A. Tarasenko, C. Reitmaier, J. Karch, D. Plohmann, Z.D. Kvon, S.D. Ganichev, Phys. Rev. B **79**, 121302 (2009)
- [109] E.L. Ivchenko, S.D. Ganichev, Pis'ma Zh. Eksp. Teor. Fiz. **93**, 752 (2007); JETP Lett. **93**, 673 (2011)
- [110] J. Karch, P. Olbrich, M. Schmalzbauer, C. Zoth, C. Brinsteiner, M. Fehrenbacher, U. Wurstbauer, M.M. Glazov, S.A. Tarasenko, E.L. Ivchenko, D. Weiss, J. Eroms, R. Yakimova, S. Lara-Avila, S. Kubatkin, S.D. Ganichev, Phys. Rev. Lett. **105**, 227402 (2010)
- [111] J. Karch, S.A. Tarasenko, E.L. Ivchenko, J. Kamann, P. Olbrich, M. Utz, Z.D. Kvon, S.D. Ganichev, Phys. Rev. B **83**, 121312 (2011)
- [112] C. Drexler, S.A. Tarasenko, P. Olbrich, J. Karch, M. Hirmer, F. Müller, M. Gmitra, J. Fabian, R. Yakimova, S. Lara-Avila, S. Kubatkin, M. Wang, R. Vajtai, P.M. Ajayan, J. Kono, S. D. Ganichev, Nat. Nanotechn. **8**, 104 (2013)
- [113] V. Lechner, L. E. Golub, F. Lomakina, V.V. Bel'kov, P. Olbrich, S. Stachel, I. Caspers, M. Griesbeck, M. Kugler, M. J. Hirmer, T. Korn, C. Schüller, D. Schuh, W. Wegscheider, S.D. Ganichev, Phys. Rev. B **83**, 155313 (2011)
- [114] P. Olbrich, C. Zoth, P. Lutz, C. Drexler, V.V. Bel'kov, Ya.V. Terent'ev, S.A. Tarasenko, A.N. Semenov, S.V. Ivanov, D.R. Yakovlev, T. Wojtowicz, U. Wurstbauer, D. Schuh, S.D. Ganichev, Phys. Rev. B **86**, 085310 (2012)
- [115] M.Z. Hasan, C.L. Kane, Rev. Modern Phys. **82**, 3045 (2010)
- [116] Y. Ando, J. Phys. Soc. Japan **82**, 102001 (2013)
- [117] I. Garate, M. Franz, Phys. Lett. **104**, 146802 (2010)
- [118] P. Hosur, Phys. Rev. B **83**, 035309 (2011)
- [119] J.W. McIver, D. Hsieh, H. Steinberg, P. Jarillo-Herrero, N. Gedik, Nat. Nanotechnol. **7**, 96 (2012)
- [120] Quan Sheng Wu, Sheng Nan Zhang, Zhong Fang, Xi Dai, Physica E **44**, 895 (2012)
- [121] P. Olbrich, L.E. Golub, T. Herrmann, S.N. Danilov, H. Plank, V.V. Bel'kov, G. Mussler, Ch. Weyrich, C.M. Schneider, J. Kampmeier, D. Grützmacher, L. Plucinski, M. Eschbach, S.D. Ganichev, Phys. Rev. Lett. **113**, 096601 (2014)
- [122] Junxi Duan, Ning Tang, Xin He, Yuan Yan, Shan Zhang, Xudong Qin, Xinqiang Wang, Xuelin Yang, Fujun Xu, Yonghai Chen, Weikun Ge, Bo Shen, Sci. Rep. **4**, 4889 (2014)
- [123] V. Kaladzhyan, P.P. Aseev, S.N. Artemenko, Phys. Rev. B **92**, 155424 (2015)
- [124] K.-M. Dantscher, D.A. Kozlov, P. Olbrich, C. Zoth, P. Faltermeier, M. Lindner, G.V. Budkin, S. A. Tarasenko, V.V. Bel'kov, Z. D. Kvon, N.N. Mikhailov, S.A. Dvoretzky, D. Weiss, B. Jenichen, S.D. Ganichev, Phys. Rev. B **92**, 165314 (2015)
- [125] Christoph Kastl, Christoph Karnetzky, Helmut Karl, A.W. Holleitner, Nat. Commun. **6**, 6617 (2015)
- [126] K.N. Okada, N. Ogawa, R. Yoshimi, A. Tsukazaki, K.S. Takahashi, M. Kawasaki, Y. Tokura, Phys. Rev. B **93**, 081403 (2016)
- [127] H. Plank, L.E. Golub, S. Bauer, V.V. Bel'kov, T. Herrmann, P. Olbrich, M. Eschbach, L. Plucinski, C.M. Schneider, J. Kampmeier, M. Lanius, G. Mussler, D. Grützmacher, S.D. Ganichev, Phys. Rev. B **93**, 125434 (2016)
- [128] H. Plank, S.N. Danilov, V.V. Bel'kov, V.A. Shalygin, J. Kampmeier, M. Lanius, G. Mussler, D. Grützmacher, and S.D. Ganichev, J. Appl. Phys. **120**, 165301 (2016)
- [129] K.-M. Dantscher, D.A. Kozlov, M.-T. Scherr, S. Gebert, J. Bärenfänger, V.V. Bel'kov, S.A. Tarasenko, M.V. Durnev, N.N. Mikhailov, S.A. Dvoretzky, Z.D. Kvon, S.D. Ganichev, *Chiral edge photogalvanic current induced in 2D HgTe topological insulators*, Int. Conf. on New Trends in Topological Insulators, Würzburg (2016)
- [130] C. Brüne, C.X. Liu, E.G. Novik, E.M. Hankiewicz, H. Buhmann, Y.L. Chen, X.L. Qi, Z.X. Shen, S.C. Zhang, L.W. Molenkamp, Phys. Rev. Lett. **106**, 126803 (2011)
- [131] D.Z. Kozlov, Z.D. Kvon, E.B. Olshanetsky, N.N. Mikhailov, S.D. Dvoretzky, D. Weiss, Phys. Rev. Lett. **112**, 196801 (2014)
- [132] F. de Juan, A.G. Grushin, T. Morimoto, J.E. Moore, Nat. Commun. **8**, 15995 (2017).
- [133] Ching-Kit Chan, N.H. Lindner, G. Refael, P.A. Lee, Photocurrents in Weyl semimetals, Phys. Rev. B **95**, 041104 (2017).
- [134] E.J. König, H.-Y. Xie, D.A. Pesin, A. Levchenko, Phys. Rev. B **96**, 075123 (2017).
- [135] L.E. Golub, E.L. Ivchenko, B.Z. Spivak, Pis'ma Zh. Eksp. Teor. Fiz. **105**, 744 (2007); JETP Lett. **105**, 782 (2017).
- [136] Q. Ma, S.-Y. Xu, C.-K. Chan, C.-L. Zhang, G. Chang, Y. Lin, W. Xie, T. Palacios, H. Lin, S. Jia, P.A. Lee, P. Jarillo-Herrero, N. Gedik, Nature Phys. **13**, 842 (2017).
- [137] Yu.I. Sirotnin, M.P. Shaskolskaya, Fundamentals of Crystal Physics (Nauka, Moscow, 1975; Mir, Moscow, 1982).